

# 1 Properdin oligomers adopt rigid extended conformations supporting 2 function

3 Dennis V. Pedersen<sup>1</sup>, Martin Nors Pedersen<sup>2</sup>, Sofia M.M. Mazarakis<sup>1</sup>, Yong Wang<sup>3</sup>, Kresten Lindorff-Larsen<sup>3</sup>,  
4 Lise Arleth<sup>2</sup>, Gregers R. Andersen<sup>1\*</sup>.

5 <sup>1</sup>Department of Molecular Biology and Genetics, Center for Structural Biology, Aarhus University, Aarhus,

6 <sup>2</sup>Structural Biophysics, X-ray and Neutron Science, the Niels Bohr Institute, University of Copenhagen,  
7 Denmark.

8 <sup>3</sup>Linderstrøm-Lang Centre for Protein Science, Department of Biology, University of Copenhagen,  
9 Copenhagen, Denmark.

10 \*Corresponding author: Gregers R. Andersen, Department of Molecular Biology and Genetics, Gustav  
11 Wieds vej 10C, DK8000 Aarhus, Denmark. Email [gra@mbg.au.dk](mailto:gra@mbg.au.dk), phone +45 30256646

12

## 13 Abstract

14 Properdin stabilizes convertases formed upon activation of the complement cascade within the immune  
15 system. The biological activity of properdin depends on the oligomerization state, but whether properdin  
16 oligomers are rigid and how their structure links to function remains unknown. We show by combining  
17 electron microscopy and solution scattering, that properdin oligomers adopt extended rigid and well-  
18 defined conformations that are well approximated by single models of apparent n-fold rotational symmetry  
19 with dimensions of 23-36 nm. Properdin monomers are pretzel shaped molecules with limited flexibility. In  
20 solution, properdin dimers are curved molecules whereas trimers and tetramers are close to being planar  
21 molecules. Structural analysis indicates that simultaneous binding through all binding sites to surface linked  
22 convertases is unlikely for properdin trimer and tetramers. We show that multivalency alone is insufficient

1 for full activity in a cell lysis assay. Hence, the observed rigid extended oligomer structure is an integral  
2 component of properdin function.

### 3 Introduction

4 The complement system is an essential aspect of innate immunity providing a first line of defense against  
5 invading pathogens as well as maintenance of host homeostasis. The complement cascade is activated  
6 when circulating pattern recognition molecules recognizes molecular patterns on a pathogen, dying host  
7 cells or immune complexes. Activation can initiate through the classical pathway (CP), the lectin pathway  
8 (LP) or the alternative pathway (AP) where the AP also provides an amplification loop for the two other  
9 pathways (1). In all three pathways, labile protein complexes known as C3 and C5 convertases are  
10 assembled. These convertases conduct proteolytic cleavage of complement component C3 and C5,  
11 respectively, resulting in the generation of opsonins (C3b and iC3b), anaphylatoxins (C3a and C5a) and  
12 assembly of the membrane attack complex (reviewed in (1)).

13 In the alternative pathway, the C3 convertase C3bBb is formed when a complex between C3b and the  
14 serine protease factor B (FB) is activated by factor D. At a high surface density of C3b, this C3 convertase  
15 becomes a C5 convertase. Properdin (FP) is a positive regulator of these convertases. FP is a 53 kDa protein  
16 composed of an N-terminal TGF- $\beta$  binding (TB) domain followed by six thrombospondin type I repeats  
17 (TSR1-6). The protein is heavily post-translationally modified carrying one N-linked glycan, four O-linked  
18 glycans and 14-17 C-mannosylated tryptophan residues in the WxxW motifs present in TSR1-6 (2,3). FP is  
19 produced predominantly by monocytes, T-cells and neutrophils and circulates as oligomers and is primarily  
20 found as dimers, trimers and tetramer with a 1:2:1 molar distribution in plasma at a concentration of 5-25  
21  $\mu\text{g/ml}$  (4,5). The functions of FP in relation to AP convertases are well established. 1) FP enhances the  
22 recruitment of FB to C3b and thereby stimulates proconvertase assembly; 2) FP slows the dissociation of  
23 C3bBb 5-10 fold; 3) FP directly competes with factor I resulting in decreased irreversible degradation of C3b  
24 to iC3b. Other suggested functions of FP are as a C3b independent pattern recognition molecule capable of  
25 triggering the AP (reviewed in (4)) and as a ligand for the NKp46 receptor on innate lymphoid cells (6). The

1 importance of FP in innate immunity and homeostasis is demonstrated by individuals with FP deficiency  
2 (PD). PD is a rare X-linked disorder which can be divided into three subtypes: type-I (complete lack of FP),  
3 type-II (1-10% of normal plasma FP level) and type-III (normal plasma level but dysfunctional FP). All PD  
4 types are characterized by reduced AP activity resulting in impaired bactericidal activity and increased  
5 susceptibility to *Neisseria* infections and sepsis (7).

6 Classic negative stain (ns) EM studies of FP dimer, trimer and tetramers revealed that FP oligomers contain  
7 compact eye shaped vertexes connected by thin connecting structures (8,9). Alcorlo and coworkers  
8 presented the first 3D reconstruction of the FP eye shaped vertices in oligomers and 2D classes of the FP-  
9 C3bBb convertase complex (10). Recently, crystallographic structures demonstrated that FP oligomers are  
10 formed upon interaction of the TB domain and TSR1 from one FP monomer with TSR4, TSR5 and TSR6 from  
11 a second FP monomer (Fig 1A). In addition, it was established that the binding site for C3b is formed by FP  
12 TSR5 in conjunction with a large loop from TSR6 (2,3,11). Despite prior attempts to analyze FP dimers and  
13 trimers with small angle X-ray scattering (SAXS) and analytical ultracentrifugation (12), detailed information  
14 regarding the structure and the dynamic properties of FP oligomers is missing. Here we present for the first  
15 time a structural description of intact oligomeric FP obtained through a combination of nsEM and SAXS.

16 Based on the recent crystal structures of monomeric FP, we are able to annotate all FP domains in  
17 monomeric, dimeric, trimeric and tetrameric FP in EM 2D classes. Pair distance distributions and atomic  
18 models based on solution scattering suggest that the FP oligomers are rather rigid in solution despite their  
19 very open structure and that their average conformations have cyclic symmetry. In addition, we  
20 demonstrate that the defined structure of FP oligomers is crucial for their biological function.

## 21 Results

### 22 The FP monomer is pretzel shaped

23 Human FP with a C-terminal His-tag was expressed by HEK293F cells and purified by affinity  
24 chromatography. The different FP oligomers were subsequently separated by cation exchange and size  
25 exclusion chromatography (SEC). As expected, both recombinant and plasma derived FP eluted in multiple

1 peaks corresponding to the different oligomerization states (Fig S1A-B). Besides dimeric, trimeric and  
2 tetrameric FP we also observed a small amount of monomeric FP (FP1) in both recombinant and plasma  
3 derived samples eluting after 14.0 ml which is similar to the elution time for the FP E244K variant described  
4 previously (11). E244K However, we were able to purify a significant amount of FP1, which allowed us to  
5 obtain negative stain EM (nsEM) data for a wild type FP monomer. The resulting 2D classes revealed a flat  
6 pretzel shaped molecule with apparent overall projected dimensions of 95x115 Å containing a small and a  
7 large ring-shaped structure sharing one edge (Fig 1B). Due to strong preference in the orientation of FP1,  
8 we could not obtain a 3D reconstruction of the molecule. Nevertheless, by analyzing nsEM 2D classes  
9 obtained for FP1 in complex with the nanobody hFPNb1 (Fig. 1C) and by comparison with the known crystal  
10 structures of FP, we could identify the positions of the individual TSRs in the 2D classes of FP1 and  
11 nanobody bound FP1. The small ring of the FP1 molecule corresponds to the well described FP “eye”  
12 formed by the TB domain, TSR1, TSR5 and TSR6 (2,3), whereas the larger ring is formed by TSR2, TSR3 and  
13 TSR4 together with the TB domain and TSR1.

14 Based on the crystal structure of the recombinant two-chain monomer FPc in which TSR3 and TSR4 are not  
15 connected (2,11), we manually constructed an atomic starting model in accordance with the FP1 2D classes  
16 and performed rigid body refinement of this model against existing SAXS data obtained for the FP1 carrying  
17 the E244K mutation (11). Distance restraints secured appropriate distances across the TSR1-TSR2, TSR3-  
18 TSR3 and TSR4-TSR4 interfaces and maintained an appropriate distance between the disulfide bridged  
19 Cys132 in TSR1 and Cys170 in TSR2. The resulting models clustered tightly and fitted the data with  $\chi^2 = 1.6$   
20 (Fig 1D-E and Fig S2B). The SAXS models strongly resembled the EM 2D classes obtained for the wt FP1  
21 monomer. The  $p(r)$  function derived from our published SAXS data FP E244K monomer (11) approaches  
22 zero at about 13 nm with a small tail stretching out to a  $D_{max}$  at 15 nm (see insert to Fig 1E). This agrees  
23 with the maximum extent of 14 nm in the nsEM 2D class projections.

1 To obtain insight into the dynamic properties of FP E244K, we conducted explicit solvent atomistic  
2 molecular dynamics simulations of a complete model of FP E244K at microsecond timescale initiating from  
3 our SAXS model obtained by rigid body modeling (Movie S1). The model included the Asn-linked complex  
4 glycan, Ser/Thr O-linked glucose-fucose, and the C-linked mannosylations on TSR tryptophans (Fig 1F). The  
5 SAXS curve calculated from the ensemble of conformations sampled by molecular dynamics simulations is  
6 in good agreement with the experimental SAXS data ( $\chi^2 = 2.2$ ). By using experimental data to guide the  
7 refinement of the conformational ensemble, the fit could be further improved to be  $\chi^2 = 1.4$  using the  
8 Bayesian Maximum Entropy (BME) method (Fig 1G). Models in this ensemble resembled the FP E244K  
9 output models from the SAXS rigid body refinement (Fig 1D) and the 2D classes obtained by EM of wild type  
10 FP1 (Fig 1B). Although the mutation E244K is expected to weaken the Trp-Arg stack in TSR3, throughout the  
11 MD simulation the Trp-Arg stack remained intact (Movie S2). However, two independent MD simulations  
12 together suggested that TSR3 inserted between TSR2 and TSR4 is capable of rotating as a rigid-body with  
13 limited conformational flexibility within domain (Fig S3C-F). This domain rotation was apparently facilitated  
14 by high mobility of the TSR4 loop region Asn285-Phe295 facing TSR3 which is in excellent agreement with  
15 weak electron density we observed for this region in two crystal structures (2). At the TSR2-TSR3 junction,  
16 the corresponding TSR3 loop Ser225-Pro237 facing TSR2 likewise exhibited flexibility (Fig S3C-D and Movie  
17 S1). For the remaining parts of FP E244K, the simulation did not indicate significant mobility, and in  
18 particular the two loops in TSR5 and TSR6 involved in convertase recognition (2,3) did not exhibit significant  
19 changes in backbone conformation (Fig S3C and Movie S1). Overall, the nsEM 2D classes for wt FP1 and the  
20 SAXS data for FP E244K provided the first quasi-atomic experimental model for the monomeric FP1 and FP  
21 E244K. Although FP1 like FP E244K probably have limited biological activity, it is present in plasma FP at  
22 very low concentrations (Fig S1B).

### 23 Pseudosymmetric FP oligomer conformations are observed by EM

24 We next analyzed the FP dimer (FP2) isolated using SEC by negative stain EM. Of the 51% of particles that  
25 were classified, 8/10 appeared in similar 2D classes suggesting that a limited number of related elliptical

1 dimer conformations are present on the EM grids (Fig 2A). The overall projected dimension of FP2 in a  
2 typical 2D class was 27×13 nm with an inner opening of 11×5 nm. However, in some classes the central  
3 opening appeared broader and the molecule less extended. At each end of the dimer, the characteristic eye  
4 shaped structure was present and the TSRs could be assigned by comparison with the 2D classes of FP1.  
5 Interestingly, TSR3 of FP2 appeared to connect TSR2 and TSR4 in an almost linear arrangement (Fig 2A)  
6 which is in contrast to the kinked conformation observed for FP1. The 2D classes suggested that the two  
7 monomers in FP2 are related by an approximate two-fold rotation axis ( $C_2$  symmetry) perpendicular to the  
8 plane of the dimer.

9 Whereas the FP2 2D classes above concurred with prior EM studies (8,10), radically different 2D classes  
10 were also obtained when hFPNb1 was included (Fig 2B). In one extreme 2D class, FP2 appeared as a folded  
11 dimer adopting a double-pretzel structure with a maximum dimension of 21 nm where the two connecting  
12 arms are crossing over at TSR3, and like in FP1, the TSR2-TSR3 angle is sharply bend (Fig 2B). This FP2  
13 conformation appeared to have a  $C_2$  symmetry axis lying in the plane of the molecule in contrast to  
14 unbound FP2 where the apparent  $C_2$  axis was perpendicular to the plane of the molecule. Other 2D classes  
15 obtained with hFPNb1 presented conformations that were intermediate between the open dimer observed  
16 in the absence of hFPNb1 and the folded dimer. A comparison of the SEC profiles supported significant  
17 conformational effects of hFPNb1 on FP2 in solution prior to EM sample preparation (Fig S1D). Importantly,  
18 hFPNb1 does not influence the oligomer distribution as shown previously (13).

19 We next analyzed the trimer FP3 by nsEM, where eight very similar 2D classes contained >90% of the  
20 particles picked (Fig 2C). In these classes, FP3 appeared in projection as flat triangular molecules with  
21 pseudo  $C_3$  symmetry having maximum edges of 28 nm with mainly straight connections formed by TSR2,  
22 TSR3 and TSR4 between the vertices. Again, when FPNb1 was present, some 2D classes contained a less  
23 planar FP3 with a maximal dimension of 24 nm where only the eye shaped vertices could be unambiguously  
24 identified (Fig 2D). Other FP3-hFPNb1 2D classes featured molecules that were flat and circular like those

1 obtained in the absence of hFPNb1 or intermediate between these two extremes. Finally, we analyzed the  
2 tetramer FP4 by nsEM and again >90% of the picked particles contributed to 2D classes with flat molecules  
3 of pseudo  $C_4$  symmetry with a maximum extent of 38 nm (Fig 2E). For both FP3 and FP4 2D classes, a kink  
4 was occasionally observed, presumably at the TSR2-TSR3 interface, in at least one of the TSR2-TSR3-TSR4  
5 connections. In summary, our nsEM analysis revealed unambiguous 2D classes for all the naturally  
6 occurring FP oligomers, and in all three cases the vast majority of classified particles were present in rather  
7 similar classes representing flat molecules with apparent  $C_n$  symmetry. Furthermore, the oligomer  
8 conformations observed in our 2D classes were not rare since the sum of particles used for the 2D classes  
9 for all three oligomers represented at least 50% of the particles picked (Fig. 2). Intriguingly, we also  
10 observed that the TSR4 specific hFPNb1 could induce alternative folded conformations of the TSR2-TSR3-  
11 TSR4 arms in FP2 and FP3 that appeared to be in equilibrium through intermediates with their elliptical and  
12 flat triangular conformations.

### 13 The solution conformation of FP oligomers

14 Taking an orthogonal approach to our nsEM analysis of the FP oligomers, we collected SEC SAXS and static  
15 SAXS data for FP2, FP3 and FP4 that was SEC fractionated prior to SAXS analysis to obtain samples  
16 optimized with respect to the relevant FP oligomer (Figs 3A-C and S2A-G). It is noteworthy that the SAXS  
17 data of all three oligomers exhibit characteristic bumps which are also reflected in their  $p(r)$ -functions (see  
18 inserts to SAXS data and fig S2H). The presence of these pronounced features clearly indicate that the  
19 oligomers are rather rigid and well-defined. If conformational freedom had been present, this would smear  
20 out the SAXS data. The  $p(r)$ -functions of FP1, FP2, FP3 and FP4 all exhibit an initial bump at around 4 nm  
21 corresponding well to the repeated distance across the eye that is also visible in the nsEM pictures of all  
22 three oligomers (see also fig S2H). The FP2 has a  $D_{max}$  value of 23 nm. Along with a second well-defined  
23 peak at around 8 nm, which is most likely related to the distance between the two antiparallel arms  
24 connecting the two eyes, the  $D_{max}$  value indicates that the FP2 solution structure is in better agreement  
25 with the extended conformation of FP2 (Fig 2A), than it is with the more compact twisted conformation

1 induced by hFPNb1 (Fig 2B). Finally, the  $p(r)$  of FP2 has a broad peak at 16.5 nm corresponding well to the  
2 distance between the two eyes. The  $D_{max}$  of the FP3 and FP4  $p(r)$  functions are, respectively, 25 and 36 nm  
3 (Fig 3B-C and Fig S2H) and in good agreement with their larger sizes also seen in the nsEM 2D classes (Figs  
4 2C and 2E). For the FP3 and FP4, the  $p(r)$  middle peak at around 8-10 nm appears broader, less pronounced  
5 and moves to higher values as the oligomer size increases. FP3 and FP4 have a high  $p(r)$  peak at 18 and 19.5  
6 nm, respectively, which is most likely the result of neighbor eye-eye distances. The increase of the eye-eye  
7 peak position when comparing FP2, FP3 and FP4 suggests that the eyes reorient towards a more planar  
8 structure as the oligomeric state increases. Furthermore, the FP4  $p(r)$  function exhibits an additional small  
9 shoulder at 28 nm which corresponds well to the less frequent diagonal eye-eye distances. For a quadratic  
10 structure, as suggested by the nsEM, these would appear at  $\sqrt{2}$  times the position of the neighbor eye-eye  
11 distances at 18-19.5 nm as they indeed do.

12 Using the same strategy and restraints as for FP1, we obtained rigid body models of FP2 in the presence of  
13  $C_1$  (no) symmetry or a  $C_2$  symmetry axis with  $\chi^2$  in the range 1.4-3.0 for  $C_1$  symmetry whereas models with  
14  $C_2$  symmetry had  $\chi^2$  of 2.4-5.5 (Fig 3A and Fig S2C). The resulting SAXS-based FP2 models all featured an  
15 extended FP2 conformation rather than the double-pretzel FP2 observed by nsEM, even if refinement was  
16 started from a double-pretzel conformation mimicking that presented in figure 2B. Interestingly, the FP2  
17 SAXS models appeared more curved as compared to the extended conformations present in EM 2D classes.  
18 In contrast to the nsEM 2D classes, the rigid body models can not be projected such that the two eye-  
19 shapes at the opposite ends of FP2 become visible simultaneously. Hence, either rigid body modelling could  
20 not reach the conformation observed in nsEM, or the FP2 conformation is influenced by the stain and  
21 contacts with the grid and therefore become excessively flat in our 2D nsEM classes. An effect of the grid is  
22 in accordance with a lower solution  $D_{max}$  compared to the maximum extent of FP2 in nsEM 2D classes.

23 Using the same strategy we generated models of FP3 and FP4 by rigid body modelling. In contrast to FP2,  
24 the  $\chi^2$  values for the fit of the best models to the experimental data were comparable and in the range 1.1-



1 1.4 indicating that the experimental data could be fitted well with single models. Importantly, the  $\chi^2$  values  
2 of the output models generated with  $C_3/C_4$  symmetry were similar to those generated with  $C_1$  symmetry  
3 demonstrating that the fit to the data was independent of symmetry (Fig 3B-C and S2D-E). All models  
4 generated with  $C_1$  symmetry were qualitatively similar extended circularized structures with their 3 or 4 eye  
5 shaped structures joined by peripheral TSR2-TSR3-TSR4 connecting arms in agreement with the FP3 and  
6 FP4 nsEM 2D classes. As for FP2, in the models generated with  $C_1$  symmetry, it was never possible to obtain  
7 projections of these SAXS models in which all eyes in FP3 and FP4 were visible. Otherwise the SAXS models  
8 had strong resemblance to the 2D classes including an occasional kink in a TSR2-TSR3-TSR4 connection (Fig  
9 3B-C). When  $C_3/C_4$  symmetry was assumed during refinement, some models were trapped in a local  
10 minimum and gave rise to highly elevated  $\chi^2$  values and models that were distinctly different from those  
11 with the lowest  $\chi^2$  values. In contrast, the best fitting models were all open and extended with TSR2-TSR3 at  
12 the periphery similar to those obtained with  $C_1$  symmetry. For some of these models, it was possible to  
13 visualize all eyes simultaneously in projections (Fig 3B-C) which is in agreement with FP3 and FP4 nsEM 2D  
14 classes. Overall, our SAXS analysis of FP oligomers were in agreement with the corresponding nsEM 2D  
15 classes and suggests that the average solution conformation of FP3 and FP4 - as expressed in the SAXS data  
16 - are well approximated by single models with  $C_3$  and  $C_4$  symmetry (S2D-E). With respect to FP2, the  
17 situation is less clear as larger differences were observed for rigid body modelling with  $C_1$  and  $C_2$  symmetry  
18 and the resulting models appear more curved than those appearing in the nsEM classes.

### 19 [The oligomerization interfaces can undergo very slow exchange](#)

20 The oligomer distribution of FP in plasma is believed to be stable after secretion, but whether monomer-  
21 monomer interactions occasionally loosen up and whether monomers may exchange between oligomers  
22 has never been addressed. Our prior purification of the two-chain monomeric FP molecules FPc and FPhtΔ3  
23 (2,11) never suggested that the two chains dissociated under native conditions. However, in size exclusion  
24 chromatography performed at low pH it was possible to separate the two FP chains (Fig. S4A) as previously  
25 demonstrated for FP oligomers (5). To investigate the stability of the FP oligomerization interfaces, we

1 mixed our two-chain monomer FPc with the two-chain deletion mutant FPht $\Delta$ 3 monomer lacking TSR3 (Fig  
2 S4B). After incubation at 37 °C, we purified FP molecules containing the His-tagged TSR4-6 tail fragment of  
3 FPht $\Delta$ 3. Using SDS-PAGE analysis, we observed that over time an increasing amount of the longer head  
4 fragment from FPc (TB-TSR1-3) co-purified with the His-tagged tail fragment from FPht $\Delta$ 3 while the amount  
5 of co-purified short FPht $\Delta$ 3 head fragment (TB-TSR1-2) decreased (Fig. S4C). Exchange between the two FP  
6 monomers was evident after 30 min and reached equilibrium after 12 hours. To examine monomer  
7 exchange into an FP oligomer, we conducted the same experiment with FP2 and FPht $\Delta$ 3. We observed that  
8 over time, an increasing amount of full length FP from FP2 co-purified with the FPht $\Delta$ 3 his-tagged TSR4-6  
9 fragment, and in this case exchange was evident after 2 hours and complete in 6-12 hours (Fig. S4D). In  
10 conclusion, these experiments for the first time demonstrated that the oligomerization interfaces in FP can  
11 open temporarily and even exchange monomers with a different FP molecule under physiologically  
12 relevant experimental conditions. However, the exchange occurs rather slowly in our pure system and is  
13 probably not a significant reaction in the extracellular environment after secretion. These results add  
14 further support to the concept of stable FP oligomer conformations.

### 15 [Convertase binding to FP oligomers](#)

16 A major outstanding question concerning FP biology is whether the strong correlation between biological  
17 activity and oligomer size is partly due to simultaneous binding to multiple C3b molecules and convertases  
18 deposited on an activator. In FP<sub>n</sub>, there are n binding sites for C3b each located at the concave face of  
19 TSR5, and our prior structures of FP-bound C3bBb revealed that C3b binds with its major axis roughly  
20 parallel to the plane of the FP eye formed by the TB domain, TSR1, TSR5 and TSR6 (14). Hence, as illustrated  
21 in Fig 3D for FP2, an oligomer with its n convertase binding sites pointing in the same direction will have the  
22 optimal architecture for binding simultaneously to n C3b molecules deposited on an activator. Due to the  
23 overall flat shape of FP oligomers, the minor principal axis is the C<sub>n</sub> rotation axis perpendicular to the plane  
24 of the models generated with C<sub>n</sub> symmetry and a pseudo n-fold rotation axis for models generated with C<sub>1</sub>  
25 symmetry (Fig 3E). We could therefore quantitate the relative orientation of the convertase binding sites in

1 our FP SAXS models by measuring the angle  $\alpha$  between an appropriate vector lying in the plane of each FP  
2 eye and the smallest principal axis of the oligomer (Fig 3E). At the maximum value,  $\alpha=180^\circ$ , the n  
3 convertase binding sites in an FP oligomer will point in the same direction and simultaneously binding at all  
4 convertase binding sites by C3b on a planar activator appears possible. At its minimum value,  $\alpha=90^\circ$ , the  
5 convertase binding sites are parallel to the plane of the FP oligomer defined by the major and intermediate  
6 principal axes and simultaneous binding to more than two C3b molecules on a planar activator appears  
7 unlikely. We observe a clear decrease in  $\alpha$  as a function of oligomer size with  $\alpha\sim 150^\circ$ ,  $128^\circ$  and  $109^\circ$  for our  
8 SAXS-based models of FP2, FP3 and FP4, respectively (Fig 3F). A decrease in  $\alpha$  with increasing multiplicity is  
9 in agreement with the shift of a major peak in the pair distance functions (Fig S2H) described above. This  
10 peak largely reflects the separation of neighboring FP eyes, and in curved oligomers this separation will be  
11 smaller than in planar oligomers.

## 12 [Oligomerization alone cannot rescue FP activity](#)

13 The activity of FP oligomers in assays exploring complement-dependent erythrocyte lysis follows the order  
14  $FP4 > FP3 > FP2$  (5), and the two chain monomer FPc and E244K FP1 are also much less active in convertase  
15 stabilization on erythrocytes and bactericidal activity compared to oligomeric FP (11). To investigate the  
16 importance of FP oligomerization and structure for activity we linked 2, 3 or 4 copies of hFPNb1 with  
17 glycine-serine linkers and showed that noncovalent FPc oligomers of increasing molecular weight linked by  
18 the multivalent hFPNb1 molecules could be formed (Fig 4A-B). Next, we compared the activity in  
19 erythrocyte lysis in FP deficient serum of free FPc and nanobody linked FPc oligomers to an FP pool  
20 containing roughly equal amounts of FP2 and FP3 (Fig S1F). As expected, the two-chain FPc monomer  
21 required a 100 fold higher concentration compared with the FP2/FP3 oligomer pool to elicit a similar  
22 degree of lysis (Fig 4C). The activity of the nanobody-linked FPc oligomers were in between the activities of  
23 the FP2/FP3 pool and FPc and increased with the hFPNb1 valency in the oligomers. The erythrocyte lysis  
24 activity of these hFPNb1 linked FPc oligomers also correlated well with their increasingly slower  
25 dissociation from a biotin-C3b sensor (Fig 4D). In conclusion, FP activity can only be partially restored by

1 linking FPc monomers through flexible linkers despite that these nanobody-linked monomers exhibited  
2 increasingly stronger binding to a C3b coated sensor compared to the FPc monomer. Hence, the well-  
3 defined extended structure of FP oligomers demonstrated by our SAXS and EM data contributes  
4 significantly to the biological activity of FP oligomers.

## 5 Discussion

6 Our demonstration of well-ordered EM 2D-classes and our ability to explain solution scattering data with  
7 single models make us suggest that FP oligomers adopt a limited number of fairly stable and overall similar  
8 conformations in solution. This is a surprising finding considering that EM 2D classes of an FP oligomer have  
9 not previously been presented and the large flexibility at especially the TSR2-TSR3 and TSR3-TSR4  
10 connections required to reach the very tight FP1 conformation (Fig 1B-D) as compared to FP crystal  
11 structures (2,3). The rigidity of FP oligomers is directly manifested by the pronounced oscillations in the  
12 SAXS data leading to well-defined peaks in the pair distance distributions (Fig 3A-C and S2H) that present  
13 sharp peaks between 15-21 nm originating from the separation of neighboring FP eyes. If the oligomers  
14 were flexible, these oscillations would be less well defined.

15 The solution structures of FP2 and FP3 were earlier investigated by Sun and coworkers with SAXS and  
16 analytical ultracentrifugation (12) and gave  $R_g$  values comparable to those presented in Fig. S2A. Their best  
17 fitting FP2 models bear weak overall resemblance to our FP2 models, but their best fitting FP3 model is  
18 rather different from the models we obtain. Furthermore, an extended model resembling our models of  
19 FP3 did not fit the scattering data in the study by Sun *et al*. One reason for these discrepancies is beyond  
20 doubt that Sun *et al* did not have a detailed model of FP to base their rigid body modelling on, and in  
21 particular they missed the crucial information regarding the stable eye structure formed by the TB domain,  
22 TSR1, TSR5 and TSR6 which we used as a single rigid body. They also used a TSR based homology model as a  
23 proxy for the N-terminal region that is a TB domain. In addition, the resolution of SAXS data in (12) was  
24 much lower with significant noise at  $q$  values above  $1 \text{ nm}^{-1}$  whereas we had only limited noise in the data in  
25 the range  $q < 2.7 \text{ nm}^{-1}$  used for rigid body refinement.

1 The binding sites for C3b is formed by FP TSR5 and TSR6 located in the FP eye and oligomerization is not  
2 strictly required for C3b binding, stimulation of C3bB assembly, inhibition of C3bBb dissociation and  
3 competition with FI. These activities are supported to some degree by the recombinant monomeric two-  
4 chain FPc molecule in which TSR2 and TSR4 are not connected by TSR3 (2,11). Furthermore, EM analysis of  
5 erythrocytes activated through the classic pathway show tight clusters of 10-40 C3b molecules extending  
6 over 40-80 nm (15), which appears well compatible with the separation of C3b/convertase binding sites  
7 observed in our structural models (Fig 3A-C).

8 Our demonstration that FP oligomers are structurally well ordered rather than dynamic modular structures  
9 (Figures 2-3) and our finding that biological activity cannot be rescued solely by linking of multiple  
10 monomeric FP molecules (Fig 4D) lead us to present a model in figure 4E for the biological function of FP  
11 oligomers. Initial monovalent binding occurs when a single FP eye engages with C3b, proconvertase or  
12 convertase. Subsequent multivalent binding is likely to be stimulated by FB binding (16) and appears  
13 feasible for neighboring convertase binding sites in all three types of oligomers and especially FP2, where  
14 the two sites are arranged favorable with respect to each other for binding parallel C3b molecules  
15 separated with an average separation of 20 nm (Fig 3D). The higher activity of FP oligomers could derive  
16 from; i) An FP oligomer simultaneously binding multiple activator-bound C3b molecules; ii) a high local  
17 concentration of C3b binding sites favoring FP rebinding after dissociation; iii) A defined 3D structure of the  
18 oligomers e.g. matching the average distribution of deposited C3b. Our prior SPR data showed a 450× lower  
19 apparent  $K_D$  value for immobilized C3b and fluid phase oligomeric FP as compared to the reverse geometry  
20 in accordance with contributions from multivalent binding and a high local concentration (11). In contrast,  
21 classic binding experiments measuring association to erythrocyte bound C3bB and zymosan-C3b complexes  
22 suggested that FP oligomers bind to a C3b opsonized activator in a monovalent fashion (16,17) arguing that  
23 the local high concentration of unbound convertase binding sites for monovalent FP-convertase  
24 interactions underlies the correlation between biological activity and oligomer stoichiometry. Our cell lysis  
25 experiments demonstrate that multivalency alone is not sufficient obtain full biological activity suggesting

1 that the defined 3D structure of the oligomers also contributes significantly to the correlation between  
2 activity and oligomer size. Although we do not know in details the oligomer distribution of FP in non-  
3 mammals, the domain structure with the TB domain followed by six thrombospondin repeats is with  
4 certainty also present in properdin sequences from amphibians, reptiles, birds, teleosts and the agnatha  
5 *Petromyzon marinus*. This evolutionary conservation supports that a defined spatial separation of  
6 convertase binding sites in FP oligomers is important for its function. For antibodies, it is known that the  
7 flexibility of the Fab-Fc hinge enables “walking” over the antigen in search for bivalent attachment on  
8 spatially defined multivalent epitopes (18,19). But since our results indicate that FP oligomers are quite  
9 rigid, these multivalent molecules seem not to be designed for “walking” over the C3b opsonized activator.  
10 Instead, the inherent flexibility of C3b and its attachment through a single covalent bond to the activator  
11 may favor multivalent FP-convertase complexes or fast rebinding through a neighboring convertase binding  
12 site (Fig 4E).

13 One reservation with respect to the model of FP structure-function relationships presented in Fig 4E is that  
14 our EM 2D classes obtained with the TSR4 binding hFPNb1 nanobody revealed intricate folded  
15 conformations and intermediates between the extended flat cyclic conformation observed in the absence  
16 of the nanobody (Fig 2B and 2D). This emphasizes, that the FP oligomer structures we present in figure 3  
17 reflect their solution conformation, but the structure may be quite different for oligomers bound to surface  
18 bound C3b and convertases on activators and NKp46 on innate lymphoid cells. The variable internal  
19 structure of TSR4 and rather different orientations of TSR4 relative to TSR5 observed in available crystal  
20 structures (2,3) and the MD simulations of FP1 presented here agrees with the ability of a TSR4 binder to  
21 induce profound conformational changes in FP oligomers. TSR4 is not directly part of the convertase  
22 binding site, but it is linked to TSR5 that harbors the majority of the convertase binding site. In an FP  
23 oligomer, a conformational signal may be relayed from TSR4 to TSR5 upon convertase binding and  
24 propagate into the rest of the oligomer. The strong preference of FP oligomers for orienting with the plane  
25 of the molecule parallel to the grid suggests that achieving high-resolution cryo-EM 3D reconstructions of

1 these unique extended structures will be an extremely challenging task. Alternatively, FP oligomers bound  
2 to a C3b or convertase coated activator model may be studied with cryo electron tomography as pioneered  
3 by Sharp and Gros for large assemblies of complement proteins (20,21).

4 Interestingly, our structures also predict that empty C3b/convertase binding sites in FP3 and FP4 point in a  
5 direction opposite to the occupied site(s) due to their  $\alpha$  angle being far from  $180^\circ$  (Fig 3F and 4E). We  
6 estimate that such unoccupied convertase binding sites in FP3 and FP4 may protrude more than 30 nm  
7 from the thioester-activator linkage of the C3b to which an existing monovalent interaction occurs (Fig 4E).  
8 Such empty binding sites appear also to be suitable for bridging a C3b opsonized cell with a second cell. The  
9 role of FP mediated agglutination – where C3b tagged bacteria lump together – in bactericidal activity is not  
10 well investigated. Historically, FP driven agglutination of erythrocytes was associated with large non-  
11 physiologically FP oligomers (22). Perhaps more relevant for *in vivo* activity, FP can also bridge C3b  
12 opsonized bacteria with host innate lymphoid cells presenting the Nkp46 receptor, an interaction shown to  
13 be required for survival in an animal model of *Neisseria meningitides* infection (6). Possibly lack of this cell-  
14 bridging function is an important element in the phenotypes of FP deficiencies in addition to compromised  
15 convertase stabilization due to weaker binding to C3b on opsonized pathogens. Interestingly,  
16 administration of recombinant FP with a high content of FP tetramers and higher oligomers was protective  
17 in mouse models of infection with *N. meningitidis* and *S. pneumonia* (23). Possibly, the bridging of bacteria  
18 and innate lymphoid cells by larger FP oligomers contributed significantly to the beneficial effects of  
19 recombinant FP administration. Very recently FP4, but not FP3 and FP2, was shown to act as a C3b  
20 independent pattern recognition molecules on bacteria binding soluble collectin 12 (24) suggesting a  
21 specialized function of FP4.

22 Our identification of FP oligomers as rigid molecules with a potential for bridging C3b opsonized cells with  
23 other cells may assist future studies analyzing the role of FP in complement driven pathogenesis and  
24 facilitate new strategies for therapeutic modulation of FP activity. Inhibition of FP by function-blocking anti-

1 mouse FP mAbs or FP gene deletion has demonstrated beneficial effects in murine models of arthritis (25),  
2 renal *ischemia-reperfusion injury (IRI)* (26), allergen-induced airway inflammation (27), abdominal aortic  
3 aneurysm (28) and atypical hemolytic uremic syndrome (29). Finally, our results should promote  
4 experiments clarifying how FP oligomers may act as C3b independent pattern recognition molecules  
5 capable of initiating the alternative pathway.

## 6 [Acknowledgements, funding sources and conflict of interest](#)

7 We thank the staff at the P12 beamline at PETRAIII for help during data collection and Karen Margrethe  
8 Nielsen and Anette Hansen for technical support. We acknowledge access to computational resources from  
9 the Danish National Supercomputer for Life Sciences (Computerome) and the ROBUST Resource for  
10 Biomolecular Simulations (supported by the Novo Nordisk Foundation). This work was supported by the  
11 Lundbeck Foundation (BRAINSTRUC, grant no. R155-2015-2666) and the Novo Nordisk Foundation  
12 (NNF16OC0022058). The authors declare no conflicts of interest in relation to this manuscript.

## 13 [Materials and methods](#)

### 14 [Protein production and SEC assays](#)

15 DNA encoding FP with C-terminal TEV-His sequence was generated by site directed mutagenesis and was  
16 expressed by transient expression in HEK293F cells as described in (11). FP was purified from cell  
17 supernatants using HisExcel column (GE Healthcare) and 1 ml Mono S column (GE Healthcare) as described  
18 (14). Fractions containing FP1, FP2, FP3 or FP4 from the Mono S column were pooled and further purified  
19 by SEC performed on a 24 mL Superdex 200 increase column (GE Healthcare) at 4 °C with a flow rate of 0.25  
20 mL/min in a buffer containing 20 mM HEPES, 150 mM NaCl pH 7.5. The monomeric FP variants FPc and  
21 FPth $\Delta$ 3 used for exchange experiments were expressed and purified as described in (2,11), respectively.  
22 hFPNb1 were expressed and purified as described in (30). SEC analysis of FPc-hFPNb1 complexes were  
23 performed with 200  $\mu$ L samples containing 14  $\mu$ g FPc in complex with hFPNb1 or its multivalent derivatives  
24 in a 4-fold molar excess with respect to the number of hFPNb1 subunits. Samples were incubated in SEC  
25 buffer at room temperature for 15 min before injection.



## 1 SAXS data acquisition, analysis and rigid body analysis

2 SAXS data was collected at the EMBL beamline P12 at PETRA III in Hamburg, Germany (31). The  
3 temperature for the sample changer and exposure unit was set to 8°C, and the detector and X-ray energy  
4 was configured to give a  $q$ -range of 0.023 to 7.332 nm<sup>-1</sup>, with  $q = 4\pi\sin(\theta)/\lambda$ , where  $\lambda$  is the wavelength  
5 of the X-ray beam and  $\theta$  is the half scattering-angle. The dimer data collected using the sample changer was  
6 inspected for radiation damage and averaged and background subtracted using primus in the ATSAS suite  
7 (Franke et al, 2017). SEC-SAXS data was collected with an in-line 24 ml Superdex 200 increase column  
8 operated at a flow rate of 0.5 ml/min. The trimer and tetramer data from SEC-SAXS were reduced using the  
9 chromixs tool from the ATSAS suite (SEC curves are presented in S2F-G). Water was used as reference to  
10 convert data to absolute scale units of cm<sup>-1</sup> (32). Initial Guinier analysis to verify that no larger aggregates  
11 were present (data not shown) and indirect Fourier transformation to determine the  $\rho(r)$  functions were  
12 performed using the BayesApp software (33) available through the “GenApp.Rocks” server maintained by  
13 Emre Brookes at University of Texas. For plotting of the scattering data, the ~800 data points were  
14 logarithmically rebinned into ~180 points with better high- $q$  statistics. Also, the data are only plotted in the  
15 fitted range out to about 0.25 Å<sup>-1</sup>. Central model independent parameters of the SAXS analysis are  
16 presented in Figure S2A.

17 Rigid body modelling of FP monomer and oligomers was performed in CORAL (34). The FP eye formed by  
18 the TB domain, TSR1, TSR4, TSR5 and TSR6 were used as a single rigid body. TSR2 and TSR3 from the crystal  
19 structure of FPc (entry 6RUS) formed two additional bodies that were linked to each other and the eye with  
20 distance restraints. In addition, an intact Asn linked complex glycan (entry 3RY6) formed a fourth rigid body  
21 linked to FP Asn428, whereas mannosyl groups linked to tryptophans and fucose-glucose disaccharides  
22 linked to serine and threonine were included in the same rigid body as the TSR domain they form a  
23 covalent bond with. The starting models were constructed such that two residues to be connected across  
24 the rigid bodies were in proximity. Starting models of FP oligomers were generated by C<sub>n</sub> symmetry and  
25 oriented with their rotation axis along the z-axis. For each FP system, six different eyes derived from entries

1 6S08, 6S0A, 6S0B, 6RUS, 6SEJ, 6RUR (2,3) were first evaluated with a consistent set of distance restraints to  
2 identify the optimal eye for the final rigid body refinements. The  $\alpha$  angle in Figure 3E-F was calculated as  
3 the angle between a vector connecting the C $\alpha$  atoms of FP residues Ala402 and Ser345 and the shortest  
4 principal axis of the SAXS rigid body models. If the average  $\alpha$  was <90, the model was flipped to yield an  
5 average  $\alpha$ >90. Ser345 and Ala402 were chosen for definition of the FP eye vector, as their difference vector  
6 is in the plane of the FP eye and roughly parallel to the long axis of the C3b in C3bBbFP complex (2).  
7 Scattering data together with an example of output model and fit to the experimental data are deposited in  
8 the SASBDB for the FP dimer, trimer and tetramer. Scattering data for the FP E244K monomer is available  
9 as SASBDB entry SASDB69.

#### 10 [Modeling and MD simulations of the FP E244K monomer](#)

11 The FP1 monomer obtained by CORAL rigid-body modeling was used as the template to construct an initial  
12 atomistic model of FP E244K with Modeller9.18 (35) in which missing residues in loops connecting domains  
13 were added and the disulfide bond Cys132-Cys170 was established. Glycosylations were added including  
14 the Asn linked-glycan at Asn428, O-linked Glucose $\beta$ 1-3Fucose at Thr92, Thr151, Ser208 and Thr272, and C-  
15 mannosylations at Trp83, Trp86, Trp139, Trp142, Trp145, Trp196, Trp199, Trp202, Trp260, Trp263, Trp321,  
16 Trp324, Trp382, Trp385, and Trp388. The glycan at Asn428 was modeled as a complex glycan. FP1 E244K  
17 was placed into a periodic cubic box with sides of 14.6 nm solvated with TIP3P water molecules containing  
18 Na<sup>+</sup> and Cl<sup>-</sup> ions at 0.15 M, resulting in ~300,000 atoms in total. The CHARMM36m force field (36) was used  
19 for the protein. Force field parameters for N- and O-linked glycans were generated using the Glycan  
20 Modeler module in the CHARMM-GUI web interface (37). Force field parameters for C-Mannosyl Trp were  
21 obtained from Shcherbakova et al. (38). Neighbor searching was performed every 20 steps. The PME  
22 algorithm was used for electrostatic interactions with a cut-off of 1.2 nm. A reciprocal grid of 128×128×128  
23 cells was used with 4th order B-spline interpolation. A single cut-off of 1.2 nm was used for Van der Waals  
24 interactions. MD simulations were performed using Gromacs 2019.4 or 2019.5 (39). The temperature and  
25 pressure were kept constant at 300 K using the Nose-Hoover thermostat and at 1.0 bar using the Parrinello-

1 Rahman barostat with a time constant of 5 ps and a frequency of 20 for coupling the pressure, respectively.  
2 Two independent MD simulations (one microsecond for each) were performed to collect the  
3 conformational ensemble. These sampled conformations were used for further ensemble refinement using  
4 the Bayesian Maximum Entropy (BME) method guided by experimental SAXS data as described (40-42). By  
5 tuning the regularization parameter in the BME reweighting algorithm, we adjusted the conformational  
6 weights in variant degrees to improve the fitting with the experimental SAXS data for FP E244K. VMD and  
7 PyMol were used for visualization of the conformational ensemble and movie preparation. The theoretical  
8 SAXS curve for each frame was back calculated using Crysol3 (43).

#### 9 [Single particle negative stain EM data acquisition and analysis](#)

10 All samples were purified on a 24 ml Superdex 200 increase size exclusion column equilibrated in 20 mM  
11 HEPES pH 7.5, 150 mM NaCl and subsequently adsorbed to glow discharged carbon coated copper grids,  
12 washed with deionized water and stained with 2 % (w/v) uranyl formate. Images were acquired with a FEI  
13 Tecnai G2 Spirit transmission microscope at 120 kV, a nominal magnification of 67.000x and a defocus  
14 ranging from 0.7 to 1.7  $\mu\text{m}$ . Automated image acquisition was performed using legion (44). For the FP1  
15 monomer and its hFPNb1 complex, CTF estimation and subsequent particle picking and extraction was  
16 carried out with cisTEM (45). For the remaining samples, CTF estimation, manual particle picking and  
17 extraction were performed with RELION (46). Initial 2D classes were generated and used to set up  
18 template-based particle picking. For all samples, 2D classification was performed in RELION.

#### 19 [FPc and FP exchange assay](#)

20 The stability of FPht $\Delta$ 3 under acidic conditions was evaluated by SEC on a 24 mL Superdex200 column (GE  
21 Healthcare) equilibrated in 20 mM HEPES, 150 mM NaCl pH 7.5 or in 100 mM glycine pH 2.3. Samples of  
22 100  $\mu\text{L}$  FPht $\Delta$ 3 at 1 mg/mL were injected and eluted at 0.5 mL/min at room temperature. Fractions were  
23 analyzed by SDS-PAGE followed by silver staining using the SilverQuest silver staining kit (Thermo Fisher).  
24 Fractions containing 0.1 M glycine pH 2.3 were neutralized with 100  $\mu\text{L}$  2 M Tris pH 8.5 before SDS-PAGE  
25 analysis. Five  $\mu\text{g}$  of FPc or dimeric FP were mixed with 5  $\mu\text{g}$  of the his-tagged FPht $\Delta$ 3 in 100  $\mu\text{L}$  of 20 mM

1 HEPES, 150 mM NaCl pH 7.5 and were incubated on ice for 5 min or at 37 °C for 5 min, 30 min, 2 h, 6 h, 12  
2 h, 24 h or 7 days. As a positive control, 5 µg of FPc or FP were mixed with 5 µg of FPhtΔ3 in 100 µL 20 mM  
3 HEPES, 150 mM NaCl pH 7.5 and subsequently acidified by adding 100 µL 0.1 M Glycine pH 2.3 to cause  
4 oligomer dissociation (5). The sample was incubated for 5 min at room temperature before 20 µL of 2M Tris  
5 pH 8.5 was added for neutralization. Pull downs were performed on all samples using 50 µL of Ni-NTA  
6 beads. The beads were transferred to a 1 mL spin columns (Bio-Rad) and equilibrated in 100 mM HEPES, 0.5  
7 M NaCl, 30 mM imidazole pH 7.5. The samples were then transferred to the columns and incubated for 2  
8 min, followed by a 30 s centrifugation step at 70 g. The beads were washed 5 times with 500 µL of 100 mM  
9 HEPES, 0.5 M NaCl, 30 mM imidazole pH 7.5 before bound protein was eluted with 80 µL of 100 mM HEPES,  
10 0.5 M NaCl, 400 mM imidazole pH 7.5. The eluates were retrieved from the columns by a 30 s  
11 centrifugation step at 70 g. The eluates were re-applied to the column and the centrifugation step was  
12 repeated. The samples were analyzed under non-reducing conditions on a 12 % SDS-PAGE gel (GenScript)  
13 using the SilverQuest silver staining kit (Invitrogen). The oligomeric FP used in this assay was approximately  
14 90 % dimer and 10 % trimer as judged by SEC analysis performed on 24 mL Superdex200 increase column  
15 (Fig. S1G). A SEC standard (Bio-Rad) was used for comparison.

#### 16 [Bio-layer interferometry assays](#)

17 Bio-layer interferometry experiments were performed on an Octet Red96 (ForteBio) at 30 °C and shaking at  
18 1,000 RPM. Binding of hFPNb1:FPc complexes were tested on streptavidin sensor tips (SA, ForteBio)  
19 equilibrated in assay buffer (PBS supplemented with 1 mg/mL BSA and 0.05 % Tween 20) and coated with  
20 biotinylated C3b at 16 µg/mL for 10 min. FPc or hFPNb1:FPc complexes were prepared by size exclusion  
21 chromatography and diluted to 50 µg FPc/mL in assay buffer. Association was monitored for 120 s followed  
22 by 120 s dissociation in assay buffer.

#### 23 [Erythrocyte lysis assay for AP activity](#)

24 Rabbit erythrocytes (Er) in 11.38 mM D-Glucose, 2.72 mM mono basic sodium citrate, 2.19 mM citric acid,  
25 7.19 mM NaCl (Alsever's Solution, Statens Seruminstitut) were washed and re-suspended in AP assay buffer

1 (5 mM barbital, 145 mM NaCl, 10 mM EGTA, 5 mM MgCl<sub>2</sub>, pH 7.4, with 0.1 % (w/v) gelatin) to obtain a 6 %  
2 (v/v) suspension. Samples of 20 µL human FP-deficient serum diluted in assay buffer and supplemented  
3 with WT FP, FPc or hFPN1-FPc complexes were prepared separately and then transferred to a V-shaped  
4 bottom 96-well microtiter plate (Nunc) in duplicates. The WT FP used for this assay was approximately 50 %  
5 dimer and 50 % trimer as judged by SEC analysis performed on a 24 mL Superdex200 increase (Fig. S1F).  
6 Ten micro liter of the E<sub>r</sub>-suspension was then transferred to the assay plate. The plate was mixed well and  
7 incubated for 2 h at 37 °C, and shaken every 30 min. Hemolysis was stopped by adding 40 µL ice-cold 0.9 %  
8 NaCl, 5 mM EDTA to each well. The plate was centrifuged at 90 *g* for 10 min, and 50 µL of each supernatant  
9 were subsequently transferred to a flat-bottom microtiter well plate (Nunc). Hemolysis was then  
10 determined from the A<sub>405</sub> measured on a Victor3 plate reader (PerkinElmer). Results are expressed relative  
11 to total hemolysis (obtained with water alone) and to background hemolysis (EDTA sample).

12

## 1 References

- 2 1. Bajic, G., Degn, S. E., Thiel, S., and Andersen, G. R. (2015) Complement activation, regulation, and  
3 molecular basis for complement-related diseases. *EMBO J* **34**, 2735-2757
- 4 2. Pedersen, D. V., Gadeberg, T. A. F., Thomas, C., Wang, Y., Joram, N., Jensen, R. K., Mazarakis, S. M.  
5 M., Revel, M., El Sissy, C., Petersen, S. V., Lindorff-Larsen, K., Thiel, S., Laursen, N. S., Fremeaux-  
6 Bacchi, V., and Andersen, G. R. (2019) Structural Basis for Properdin Oligomerization and  
7 Convertase Stimulation in the Human Complement System. *Front Immunol* **10**, 2007
- 8 3. van den Bos, R. M., Pearce, N. M., Granneman, J., Brondijk, T. H. C., and Gros, P. (2019) Insights Into  
9 Enhanced Complement Activation by Structures of Properdin and Its Complex With the C-Terminal  
10 Domain of C3b. *Front Immunol* **10**, 2097
- 11 4. Blatt, A. Z., Pathan, S., and Ferreira, V. P. (2016) Properdin: a tightly regulated critical inflammatory  
12 modulator. *Immunol Rev* **274**, 172-190
- 13 5. Pangburn, M. K. (1989) Analysis of the natural polymeric forms of human properdin and their  
14 functions in complement activation. *Journal of immunology* **142**, 202-207
- 15 6. Narni-Mancinelli, E., Gauthier, L., Baratin, M., Guia, S., Fenis, A., Deghmane, A. E., Rossi, B.,  
16 Fourquet, P., Escaliere, B., Kerdiles, Y. M., Ugolini, S., Taha, M. K., and Vivier, E. (2017) Complement  
17 factor P is a ligand for the natural killer cell-activating receptor NKp46. *Sci Immunol* **2**
- 18 7. Skattum, L., van Deuren, M., van der Poll, T., and Truedsson, L. (2011) Complement deficiency  
19 states and associated infections. *Mol Immunol* **48**, 1643-1655
- 20 8. Smith, C. A., Pangburn, M. K., Vogel, C. W., and Muller-Eberhard, H. J. (1984) Molecular  
21 architecture of human properdin, a positive regulator of the alternative pathway of complement. *J*  
22 *Biol Chem* **259**, 4582-4588
- 23 9. Higgins, J. M., Wiedemann, H., Timpl, R., and Reid, K. B. (1995) Characterization of mutant forms of  
24 recombinant human properdin lacking single thrombospondin type I repeats. Identification of  
25 modules important for function. *Journal of immunology* **155**, 5777-5785
- 26 10. Alcorlo, M., Tortajada, A., Rodriguez de Cordoba, S., and Llorca, O. (2013) Structural basis for the  
27 stabilization of the complement alternative pathway C3 convertase by properdin. *Proc Natl Acad*  
28 *Sci U S A* **110**, 13504-13509
- 29 11. Pedersen, D. V., Roumenina, L., Jensen, R. K., Gadeberg, T. A., Marinozzi, C., Picard, C., Rybkine, T.,  
30 Thiel, S., Sorensen, U. B., Stover, C., Fremeaux-Bacchi, V., and Andersen, G. R. (2017) Functional and  
31 structural insight into properdin control of complement alternative pathway amplification. *EMBO J*  
32 **36**, 1084-1099
- 33 12. Sun, Z., Reid, K. B., and Perkins, S. J. (2004) The dimeric and trimeric solution structures of the  
34 multidomain complement protein properdin by X-ray scattering, analytical ultracentrifugation and  
35 constrained modelling. *J Mol Biol* **343**, 1327-1343
- 36 13. Pedersen, D. V., Rosner, T., Hansen, A. G., Andersen, K. R., Thiel, S., Andersen, G. R., Valerius, T.,  
37 and Laursen, N. S. (2020) Recruitment of properdin by bi-specific nanobodies activates the  
38 alternative pathway of complement. *Mol Immunol* **124**, 200-210
- 39 14. Pedersen, D. V., Revel, M., Gadeberg, T. A. F., and Andersen, G. R. (2019) Crystallization and X-ray  
40 analysis of monodisperse human properdin. *Acta Crystallogr F Struct Biol Commun* **75**, 0
- 41 15. Mardiney, M. R., Jr., Muller-Eberhard, H. J., and Feldman, J. D. (1968) Ultrastructural localization of  
42 the third and fourth components of complement on complement-cell complexes. *Am J Pathol* **53**,  
43 253-261
- 44 16. DiScipio, R. G. (1981) The binding of human complement proteins C5, factor B, beta 1H and  
45 properdin to complement fragment C3b on zymosan. *Biochem J* **199**, 485-496
- 46 17. Farries, T. C., Lachmann, P. J., and Harrison, R. A. (1988) Analysis of the interactions between  
47 properdin, the third component of complement (C3), and its physiological activation products.  
48 *Biochem J* **252**, 47-54

- 1 18. Zhang, P., Liu, X., Liu, P., Wang, F., Ariyama, H., Ando, T., Lin, J., Wang, L., Hu, J., Li, B., and Fan, C.  
2 (2020) Capturing transient antibody conformations with DNA origami epitopes. *Nat Commun* **11**,  
3 3114
- 4 19. Preiner, J., Kodera, N., Tang, J., Ebner, A., Brameshuber, M., Blaas, D., Gelbmann, N., Gruber, H. J.,  
5 Ando, T., and Hinterdorfer, P. (2014) IgGs are made for walking on bacterial and viral surfaces. *Nat*  
6 *Commun* **5**, 4394
- 7 20. Sharp, T. H., Boyle, A. L., Diebold, C. A., Kros, A., Koster, A. J., and Gros, P. (2019) Insights into  
8 IgM-mediated complement activation based on in situ structures of IgM-C1-C4b. *Proc Natl Acad Sci*  
9 *U S A* **116**, 11900-11905
- 10 21. Sharp, T. H., Koster, A. J., and Gros, P. (2016) Heterogeneous MAC Initiator and Pore Structures in a  
11 Lipid Bilayer by Phase-Plate Cryo-electron Tomography. *Cell Rep* **15**, 1-8
- 12 22. Farries, T. C., Finch, J. T., Lachmann, P. J., and Harrison, R. A. (1987) Resolution and analysis of  
13 'native' and 'activated' properdin. *Biochem J* **243**, 507-517
- 14 23. Ali, Y. M., Hayat, A., Saeed, B. M., Haleem, K. S., Alshamrani, S., Kenawy, H. I., Ferreira, V. P., Saggu,  
15 G., Buchberger, A., Lachmann, P. J., Sim, R. B., Goundis, D., Andrew, P. W., Lynch, N. J., and  
16 Schwaeble, W. J. (2014) Low-dose recombinant properdin provides substantial protection against  
17 *Streptococcus pneumoniae* and *Neisseria meningitidis* infection. *Proc Natl Acad Sci U S A* **111**, 5301-  
18 5306
- 19 24. Zhang, J., Song, L., Pedersen, D. V., Li, A., Lambris, J. D., Andersen, G. R., Mollnes, T. E., Ma, Y., and  
20 Garred, P. (2020) Soluble collectin-12 mediates C3-independent docking of properdin that activates  
21 the 1 alternative pathway of complement. *eLife* **Accepted**
- 22 25. Kimura, Y., Zhou, L., Miwa, T., and Song, W. C. (2010) Genetic and therapeutic targeting of  
23 properdin in mice prevents complement-mediated tissue injury. *J Clin Invest* **120**, 3545-3554
- 24 26. Miwa, T., Sato, S., Gullipalli, D., Nangaku, M., and Song, W. C. (2013) Blocking properdin, the  
25 alternative pathway, and anaphylatoxin receptors ameliorates renal ischemia-reperfusion injury in  
26 decay-accelerating factor and CD59 double-knockout mice. *Journal of immunology* **190**, 3552-3559
- 27 27. Wang, Y., Miwa, T., Ducka-Kokalar, B., Redai, I. G., Sato, S., Gullipalli, D., Zangrilli, J. G., Haczku, A.,  
28 and Song, W. C. (2015) Properdin Contributes to Allergic Airway Inflammation through Local C3a  
29 Generation. *Journal of immunology* **195**, 1171-1181
- 30 28. Bertram, P., Akk, A. M., Zhou, H. F., Mitchell, L. M., Pham, C. T., and Hourcade, D. E. (2015) Anti-  
31 mouse properdin TSR 5/6 monoclonal antibodies block complement alternative pathway-  
32 dependent pathogenesis. *Monoclon Antib Immunodiagn Immunother* **34**, 1-6
- 33 29. Ueda, Y., Miwa, T., Gullipalli, D., Sato, S., Ito, D., Kim, H., Palmer, M., and Song, W. C. (2018)  
34 Blocking Properdin Prevents Complement-Mediated Hemolytic Uremic Syndrome and Systemic  
35 Thrombophilia. *J Am Soc Nephrol* **29**, 1928-1937
- 36 30. Jensen, R. K., Pihl, R., Gadeberg, T. A. F., Jensen, J. K., Andersen, K. R., Thiel, S., Laursen, N. S., and  
37 Andersen, G. R. (2018) A potent complement factor C3-specific nanobody inhibiting multiple  
38 functions in the alternative pathway of human and murine complement. *J Biol Chem* **293**, 6269-  
39 6281
- 40 31. Blanchet, C. E., Spilotros, A., Schwemmer, F., Graewert, M. A., Kikhney, A., Jeffries, C. M., Franke,  
41 D., Mark, D., Zengerle, R., Cipriani, F., Fiedler, S., Roessle, M., and Svergun, D. I. (2015) Versatile  
42 sample environments and automation for biological solution X-ray scattering experiments at the  
43 P12 beamline (PETRA III, DESY). *J Appl Crystallogr* **48**, 431-443
- 44 32. Orthaber, D., Bergmann, A., and Glatter, O. (2000) SAXS experiments on absolute scale with Kratky  
45 systems using water as a secondary standard. *Journal of Applied Crystallography* **33**, 218-225
- 46 33. Hansen, S. (2012) BayesApp: a web site for indirect transformation of small-angle scattering data.  
47 *Journal of Applied Crystallography* **45**, 566-567
- 48 34. Petoukhov, M. V., Franke, D., Shkumatov, A. V., Tria, G., Kikhney, A. G., Gajda, M., Gorba, C.,  
49 Mertens, H. D., Konarev, P. V., and Svergun, D. I. (2012) New developments in the ATSAS program  
50 package for small-angle scattering data analysis. *J Appl Crystallogr* **45**, 342-350



- 1 35. Webb, B., and Sali, A. (2016) Comparative Protein Structure Modeling Using MODELLER. *Curr Protoc*  
2 *Bioinformatics* **54**, 5 6 1-5 6 37
- 3 36. Huang, J., Rauscher, S., Nawrocki, G., Ran, T., Feig, M., de Groot, B. L., Grubmuller, H., and  
4 MacKerell, A. D., Jr. (2017) CHARMM36m: an improved force field for folded and intrinsically  
5 disordered proteins. *Nat Methods* **14**, 71-73
- 6 37. Park, S. J., Lee, J., Qi, Y., Kern, N. R., Lee, H. S., Jo, S., Joung, I., Joo, K., Lee, J., and Im, W. (2019)  
7 CHARMM-GUI Glycan Modeler for modeling and simulation of carbohydrates and glycoconjugates.  
8 *Glycobiology* **29**, 320-331
- 9 38. Shcherbakova, A., Preller, M., Taft, M. H., Pujols, J., Ventura, S., Tiemann, B., Buettner, F. F., and  
10 Bakker, H. (2019) C-mannosylation supports folding and enhances stability of thrombospondin  
11 repeats. *Elife* **8**
- 12 39. Abraham, M. J., Murtola, T., Schulz, R., Páll, S., Smith, J. C., Hess, B., and Lindahl, E. (2015)  
13 GROMACS: High performance molecular simulations through multi-level parallelism from laptops to  
14 supercomputers. *SoftwareX* **1-2**, 19-25
- 15 40. Weinhaupl, K., Lindau, C., Hessel, A., Wang, Y., Schutze, C., Jores, T., Melchionda, L., Schonfisch, B.,  
16 Kalbacher, H., Bersch, B., Rapaport, D., Brennich, M., Lindorff-Larsen, K., Wiedemann, N., and  
17 Schanda, P. (2018) Structural Basis of Membrane Protein Chaperoning through the Mitochondrial  
18 Intermembrane Space. *Cell* **175**, 1365-1379 e1325
- 19 41. Orioli, S., Larsen, A. H., Bottaro, S., and Lindorff-Larsen, K. (2020) How to learn from  
20 inconsistencies: Integrating molecular simulations with experimental data. *Prog Mol Biol Transl Sci*  
21 **170**, 123-176
- 22 42. Bottaro, S., Bengtsen, T., and Lindorff-Larsen, K. (2020) Integrating Molecular Simulation and  
23 Experimental Data: A Bayesian/Maximum Entropy Reweighting Approach. *Methods Mol Biol* **2112**,  
24 219-240
- 25 43. Franke, D., Petoukhov, M. V., Konarev, P. V., Panjkovich, A., Tuukkanen, A., Mertens, H. D. T.,  
26 Kikhney, A. G., Hajizadeh, N. R., Franklin, J. M., Jeffries, C. M., and Svergun, D. I. (2017) ATSAS 2.8: a  
27 comprehensive data analysis suite for small-angle scattering from macromolecular solutions. *J Appl*  
28 *Crystallogr* **50**, 1212-1225
- 29 44. Carragher, B., Kisseberth, N., Kriegman, D., Milligan, R. A., Potter, C. S., Pulokas, J., and Reilein, A.  
30 (2000) Leginon: An automated system for acquisition of images from vitreous ice specimens. *J*  
31 *Struct Biol* **132**, 33-45
- 32 45. Grant, T., Rohou, A., and Grigorieff, N. (2018) cisTEM, user-friendly software for single-particle  
33 image processing. *Elife* **7**
- 34 46. Scheres, S. H. W. (2012) RELION: Implementation of a Bayesian approach to cryo-EM structure  
35 determination. *J Struct Biol* **180**, 519-530

36



## 1 Figure Legends

2 **Figure 1. Principles of properdin architecture and the structure of FP1.** A) Schematic representation of the  
3 FP1 monomer and FP2 as an example of an oligomer, where one subunit is colored grey while the other is  
4 colored according to the domain structure as for FP1. B) The 10 most populated nsEM 2D classes obtained  
5 with FP1 with the number of particles indicated. A magnified view of the 2D class marked by star is shown  
6 to the right. C) As for panel B, but for the FP1-hFPNb1 complex. Compared to FP1, an additional mass marks  
7 the location of hFPNb1 and hence TSR4 enabling assignment of the TB domain and the six thrombospondin  
8 repeats in the magnified view to the right. D) Representative atomic model of FP1 E244K derived by rigid  
9 body modelling against the SAXS data. E) Comparison of SAXS experimental data (11) and the fitted  
10 scattering curve corresponding to the FP1 E244K model presented in panel E. Insert to E:  $\rho(r)$  function  
11 derived from the SAXS data. F) Conformational ensemble of FP1 E244K sampled by a one  $\mu$ s MD simulation  
12 represented by 100 frames with 10 ns interval shown as transparent tubes. The starting model is displayed  
13 as a cartoon with the glycans and glycosylated residues in grey stick representation. Disulfide bridges are  
14 represented by yellow sticks. G) Comparison of SAXS experimental data and the scattering curve obtained  
15 from MD ensemble after refinement using the Bayesian maximum entropy approach, the two curves fit  
16 with  $\chi^2 = 1.4$ . The minor difference in the experimental data apparent at the highest q-values in panels E  
17 and G is due to subtraction of a constant by CORAL in panel E.

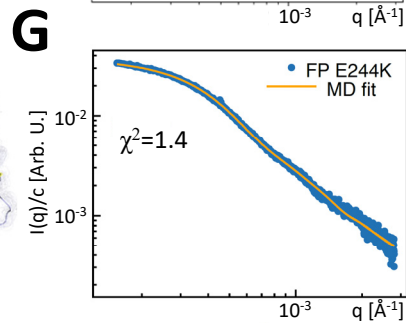
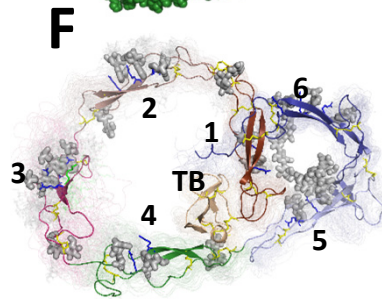
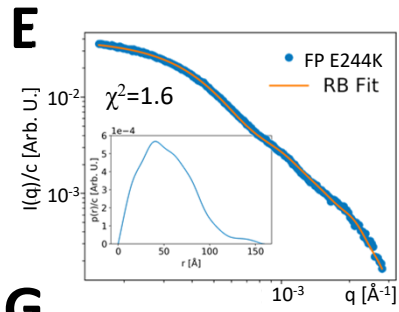
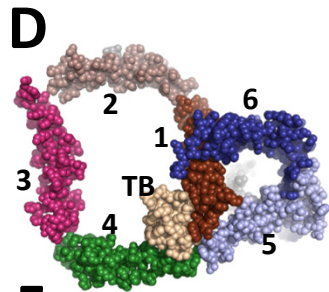
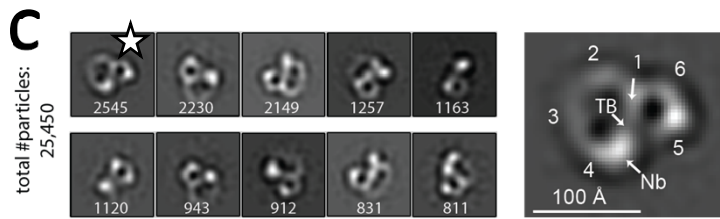
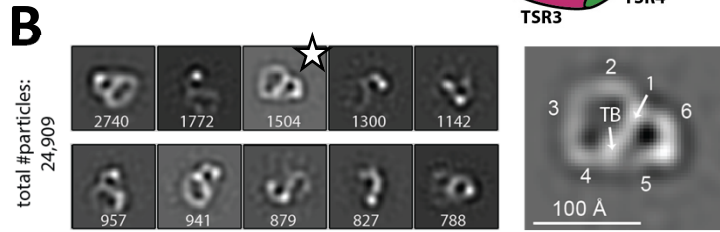
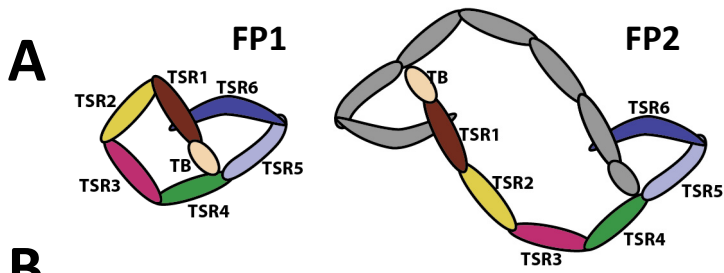
18 **Figure 2. Negative stain EM analysis of FP oligomers.** For all cases, the 10 most populated nsEM 2D classes  
19 obtained are displayed with the number of particles indicated. A). The 2D classes obtained with FP2 and a  
20 magnified view of the 2D class marked by star is shown to the right with the putative domain assignment  
21 indicated for one of the two monomers in the dimer. Notice the difference in curvature at TSR2 and TSR4 of  
22 the connecting arms, which facilitates the domain assignment. B) As panel A, but with the FP2-hFPNb1  
23 complex. The double pretzel conformation is present in two classes, while others feature the elliptical  
24 shape or intermediates. C) The 2D classes obtained with FP3 reveal a flat molecule structure of apparent  $C_3$   
25 symmetry. D) The FP3-hFPNb1 complex. The 2D class to the left reveals an FP3 conformation with an

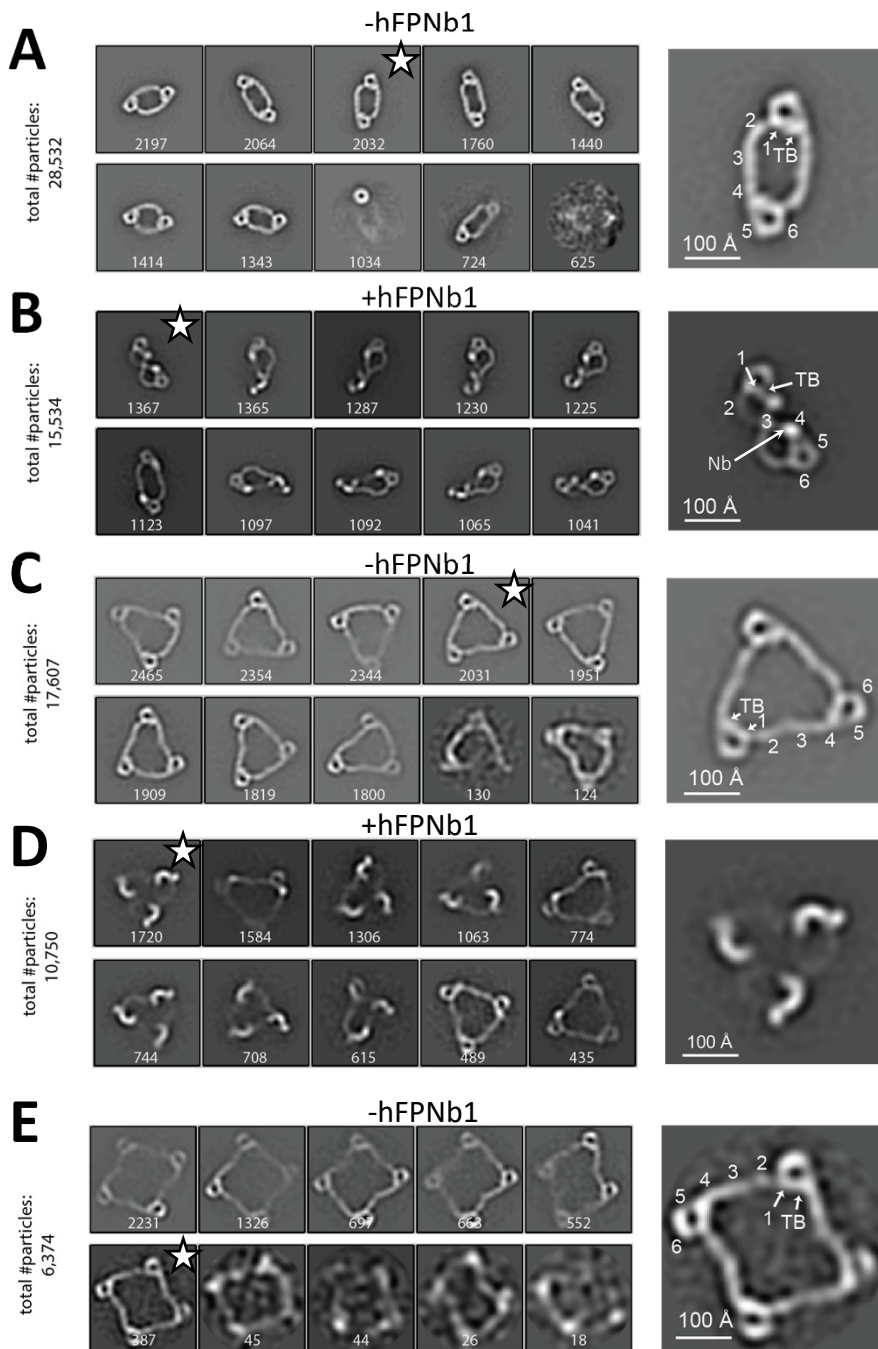
1 apparent  $C_3$  symmetry that is radically different from the cyclic appearance of FP3 in panel C, but 2D classes  
2 presenting flat cyclic FP3 and intermediates are also present. E) The 2D classes obtained with FP4 suggest a  
3 planar extended molecule with apparent  $C_4$  symmetry.

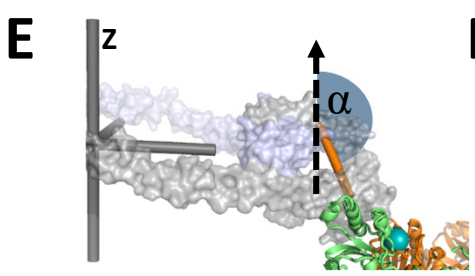
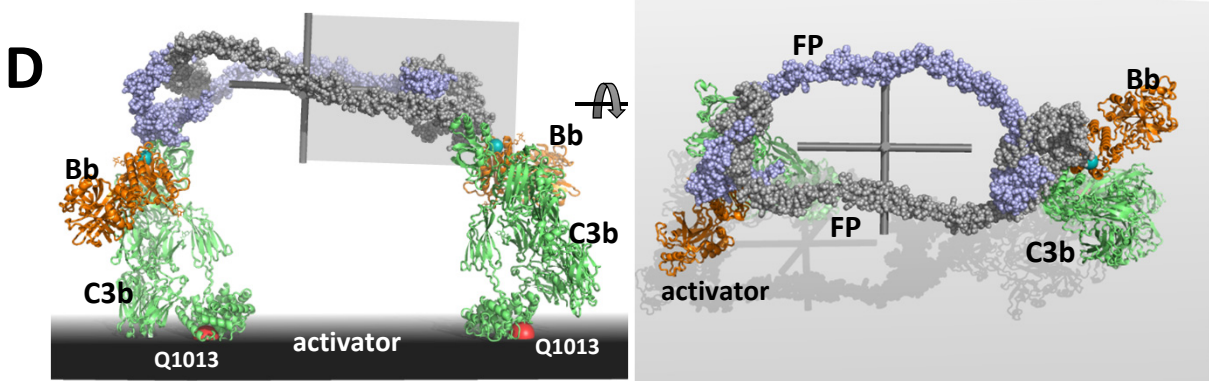
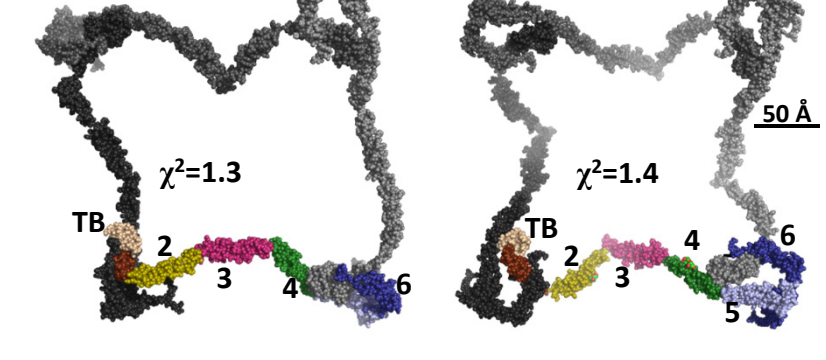
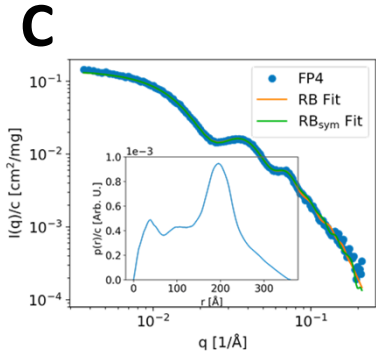
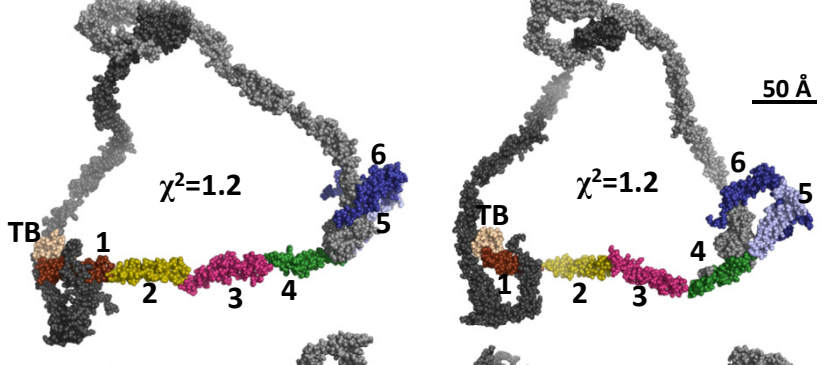
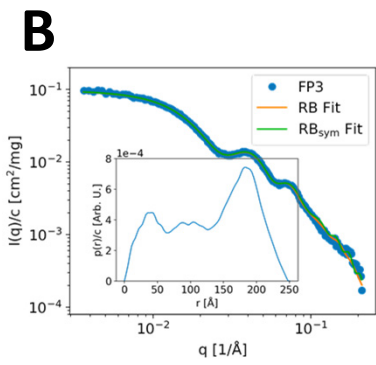
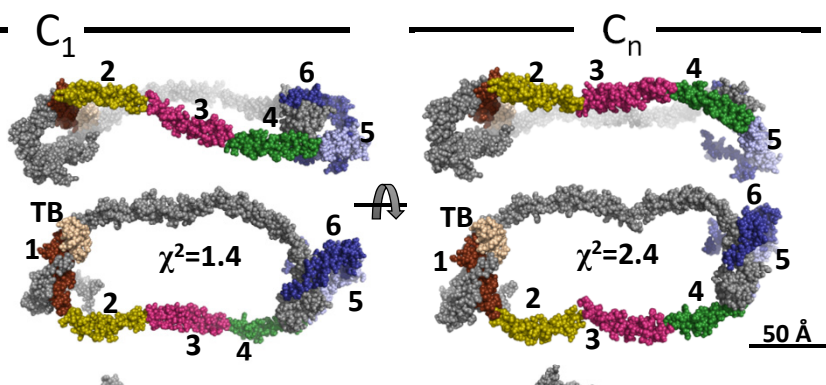
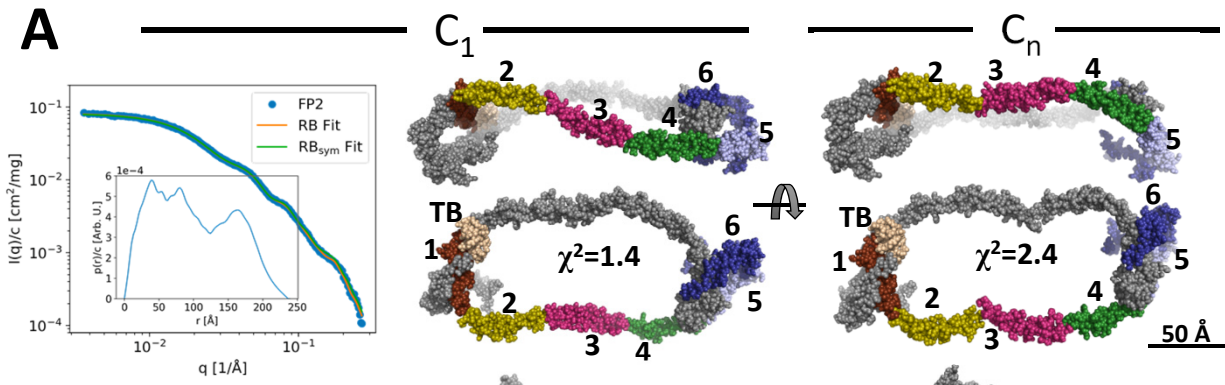
4 **Figure 3. Models of FP oligomers obtained by SAXS rigid body refinement.** A-C) Left: SAXS data (blue) and  
5 model fits (orange) corresponding to FP2, FP3 and FP4 structures obtained with  $C_1$  symmetry. Inserts plot  
6 the corresponding  $p(r)$  functions. Middle: Models fitted using  $C_1$  symmetry. Right: Models fitted assuming  
7  $C_n$  symmetry. The  $C_1$  models were chosen as the most representative model in the largest cluster from the  
8 10 generated, whereas the  $C_n$  models were those amongst 10 or 30 models that according to their  $\chi^2$  value  
9 were in best agreement with the experimental data, see panel F. In panel A, two orientations are displayed  
10 to illustrate the curvature of FP2 models. D) Hypothetical model of FP2 from panel A bound to two C3  
11 convertases to illustrate that such a complex could be formed on an activator to which the two C3b  
12 molecules (green) carrying the Bb protease (orange) are bound through their Gln1013 (red sphere). The  
13 two FP monomers are colored light blue and grey, respectively. To the left is presented a side view and to  
14 the right a top view. The principal axes of FP2 are displayed as a grey Cartesian coordinate system. E)  
15 Enlarged view of the area outlined with a grey box in panel D. The vertical dashed vector is parallel to the  
16 smallest principal axis (labelled "z") of the FP2 molecule, the orange stick represents the vector in the plane  
17 of the FP eye used for calculation of  $\alpha$ , the angle between the two vectors. F) The average  $\alpha$  values  
18 calculated from the SAXS rigid body models. The number of models used for statistics from a pool of 10 or  
19 30 models is indicated by the number n, remaining models were discarded as they had  $\chi^2$  values that were  
20 significantly higher than the n well fitting models.

21 **Figure 4. The biological activity of nanobody linked FP oligomers is lower than that of an FP2/FP3**  
22 **oligomer pool.** A) SEC profiles showing that hFPNb1 oligomers form stable oligomers with FPc. B) SDS-PAGE  
23 analysis of the peak fraction from each SEC experiments in panel A confirming that all hFPNb1 variants form  
24 stable complexes with FPc. C) Assay where lysis of rabbit erythrocytes (% of lysis in pure water) in FP

1 depleted serum is used as a measure of AP activity. Erythrocyte lysis is shown as a function of protein  
2 concentration. The ability to induce erythrocyte lysis clearly increases with increasing hFPNb1 mediated  
3 oligomerization of FPc. Each point corresponds to the average of two independent experiments, both  
4 performed in technical duplicates. The error bars represent the standard deviation between the two  
5 independent experiments. D) Biolayer interferometry sensorgrams showing the binding of FPc (blue) or  
6 preformed FPc-hFPNb1 monomers (green), dimers (purple), trimers (orange), or tetramers (red) to a C3b  
7 coated sensor. The sensorgrams demonstrate that binding of hFPNb1 mediated FPc oligomers to C3b is  
8 stronger than for the monomeric FPc or the FPc-hFPNb1 complex. In particular, the dissociation rate is  
9 observed to be strongly dependent on hFPNb1 valency. E) Model of FP structure-functions relationships  
10 using FP4 as example. To the left, one convertase binding site is occupied, a neighboring binding site may  
11 form contact with a nearby C3b, proconvertase or convertase. Flexibility of C3b due to the single bond  
12 attachment to the activator may favor FP interaction with the second C3b molecule. Right, FP convertase  
13 binding sites not pointing towards the activator surface reach >30 nm into solution and appear as ideal for  
14 bridging C3b opsonized pathogens with NKp46 presenting innate lymphoid cells. Notice that the NKp46  
15 binding site on FP is presently unknown.



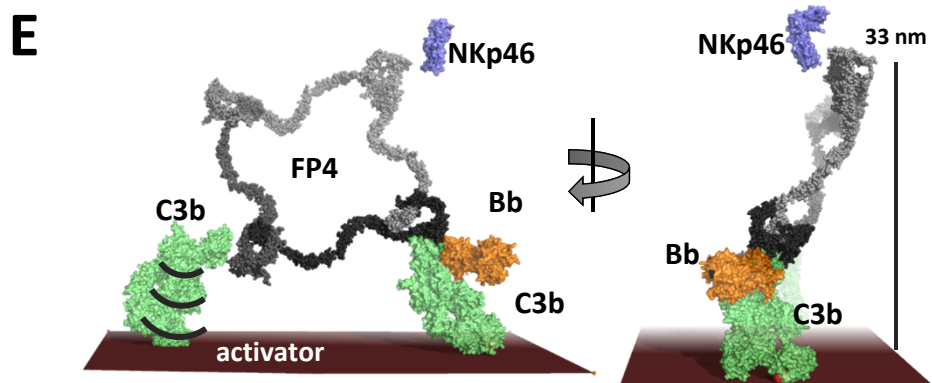
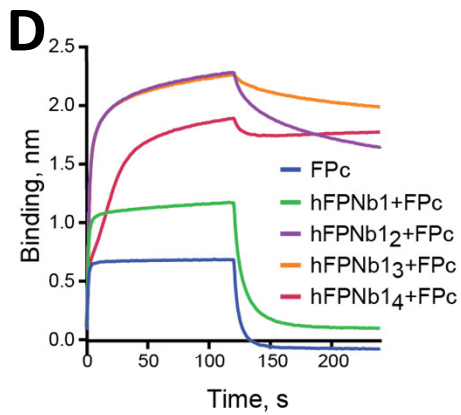
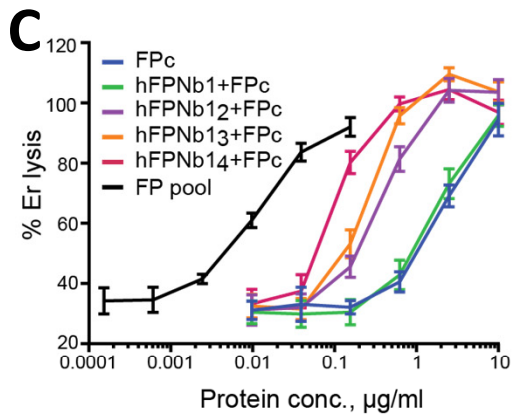
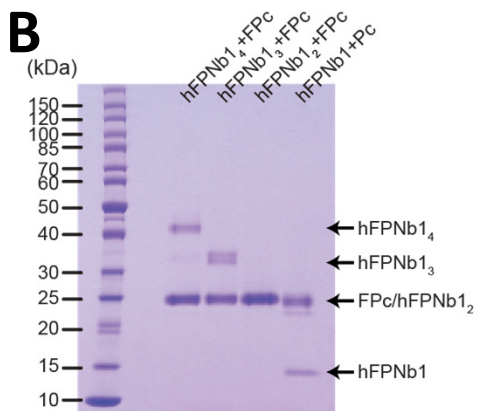
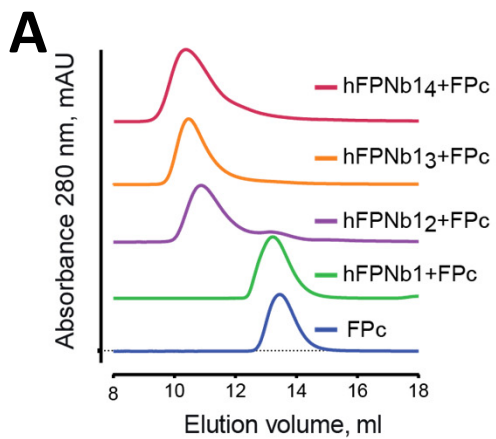




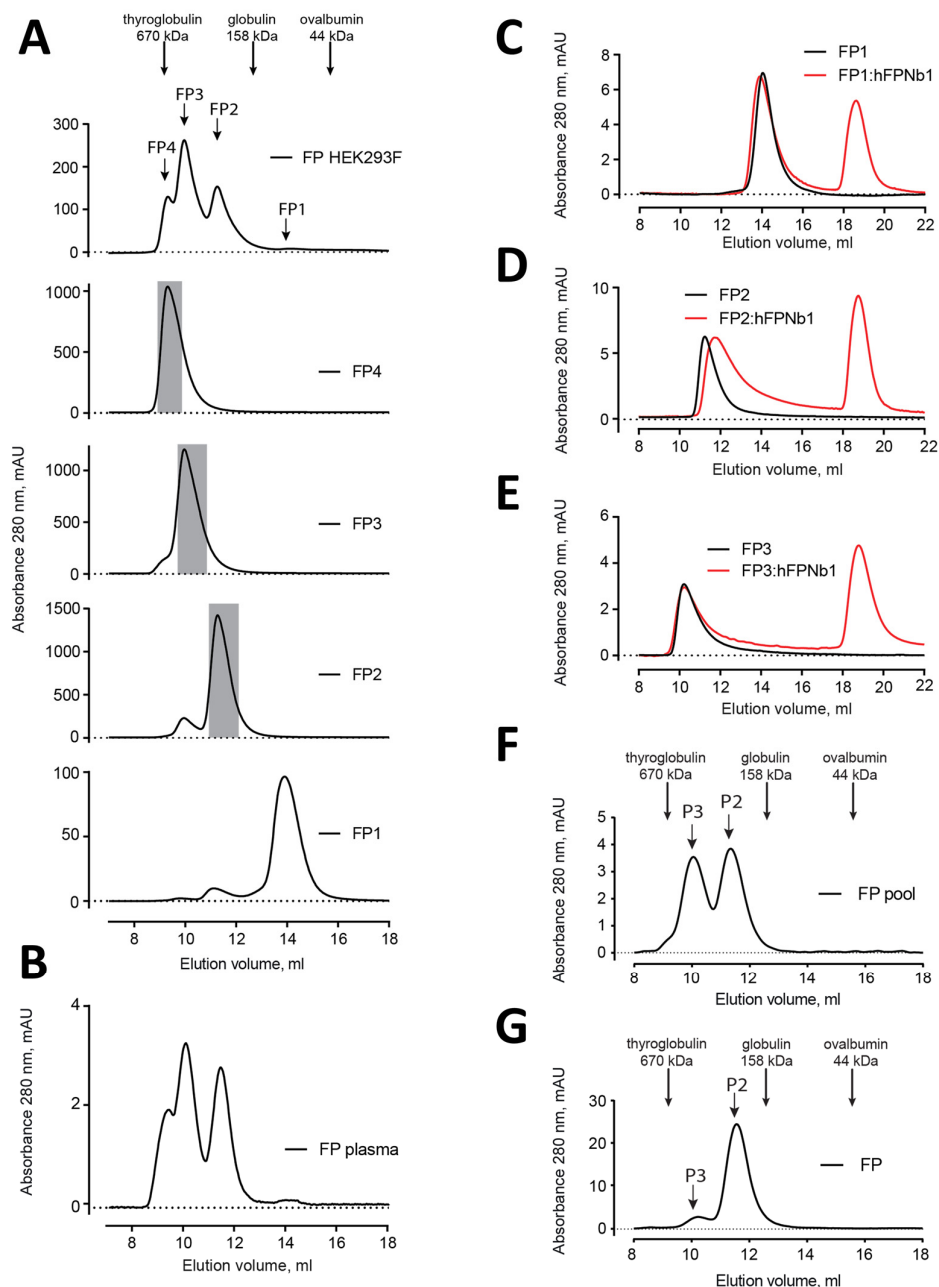
**F**

	$C_1$	$C_n$
FP2	147±17 n=8/10	152±8 n=8/10
FP3	136±19 n=10/10	121±14 n=11/30
FP4	113±26 n=10/10	105±12 n=20/30





## Supporting Information

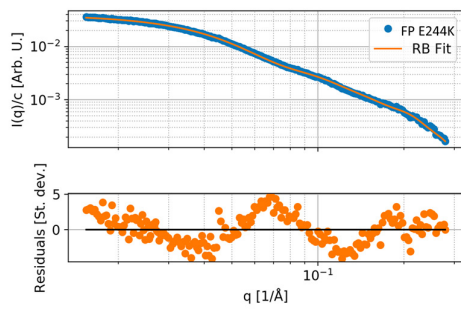
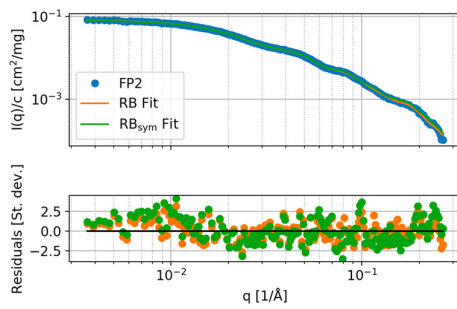
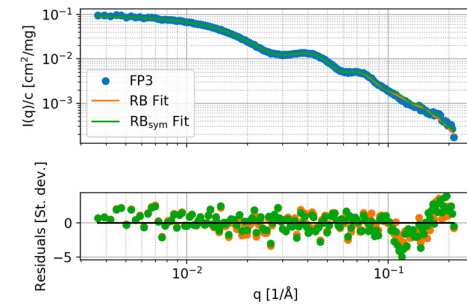
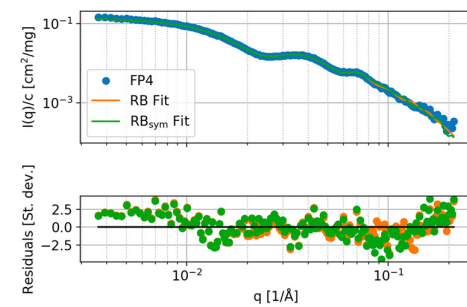
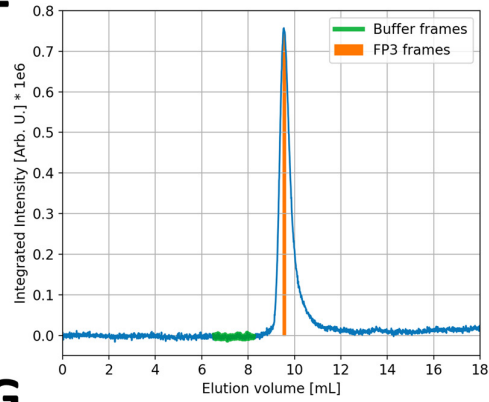
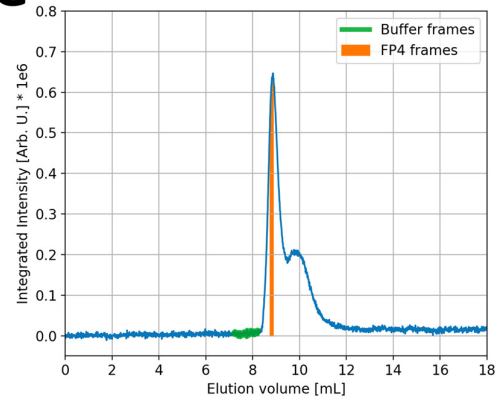
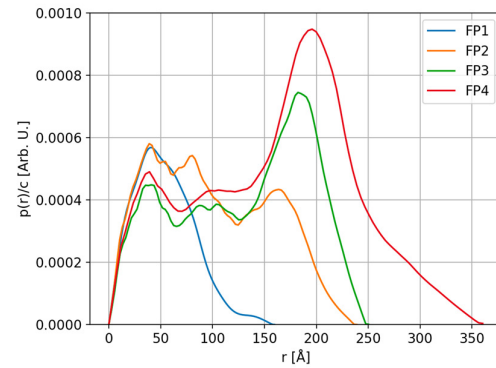


**Figure S1. Elution profiles of recombinant FP.** A) Top, SEC analysis of initial pool of recombinant FP obtained by His<sub>6</sub> based affinity chromatography. Below is presented SEC profiles for the final purification step of recombinant FP1, FP2, FP3 and FP4 obtained from HEK293F cells used for SAXS data collection and negative stain EM (greyed areas). B) SEC profile of commercial plasma FP for comparison. C-E) SEC analysis of FP1, FP2, and FP3 with or without hFPNb1 used for nsEM in figures 1 and 2. F-G) SEC analysis of the FP2/FP3 pool and a pool dominated by FP2 used for the functional assays in figure 4 and exchange experiments in figure S4, respectively.



**A**

Sample	Concentration [mg·mL <sup>-1</sup> ]	I(0) [1/cm]	MW <sub>exp</sub> (kDa)	MW <sub>nom</sub> (kDa)	R <sub>g</sub> [Å]	Dmax [Å]
FP2	1.92	0.16	112	110	81+/- 1	234
FP3	0.47	4.61E-02 +/- 4E-04	135	165	102+/- 1	245
FP4	0.37	5.47E-02 +/- 4E-04	208	220	126+/- 1	356

**B****C****D****E****F****G****H**

**Figure S2. SAXS data.** A) Model independent parameters of the SAXS analysis. Forward scattering intensity,  $I(0)$ , in absolute units of  $\text{cm}^{-1}$ .  $MW_{\text{exp}}$ : Average MW of the oligomer as derived from the forward scattering and the protein concentration. The uncertainty of the MW determination is expected to be around 10% for the FP2 which was measured using the sample changer setup and around 20% for the SEC-SAXS based setup. When taking this into account, the experimental MW-values compare well with their nominal values,  $MW_{\text{nom}}$ , calculated using a monomer MW of 55 kDa.  $R_g$ : Radius of gyration and  $D_{\text{max}}$ : Maximal distance of the  $p(r)$ . The  $I(0)$ ,  $R_g$  and  $D_{\text{max}}$  are derived from the Indirect Fourier Transformation as described in the materials and methods section. B-E) Experimental SAXS data (blue points), fit of rigid body (RB) model (orange full line) and fit of  $C_n$  symmetric model with  $n=2$  (FP2), 3 (FP3) and 4 (FP4), respectively, in panels C, D and E (green full line). Corresponding residual plots are presented underneath each SAXS plot. F-G) Integrated SAXS intensity of the SEC-SAXS data obtained for FP3 and FP4. The frames used for the foreground (FP3/4 frames) and buffer frames selected for the background are indicated on the plots. H) Direct comparison of the  $p(r)$  functions obtained from the SAXS data on FP1 E244K, FP2, FP3 and FP4.

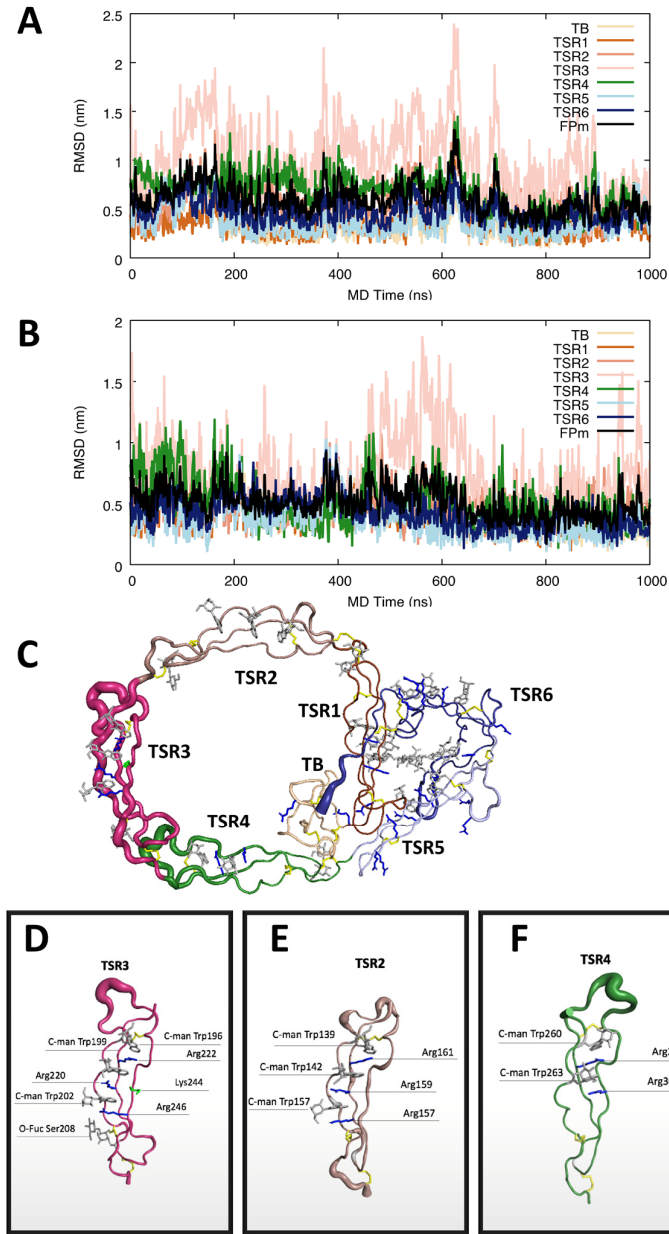


**Figure S3. Molecular dynamics simulation of the FP1 E244K.** A-B) The root mean square deviation (RMSD) of each domain and the whole protein with the trajectories aligned to the initial FP1 E244K model in two independent one  $\mu$ s MD simulations. Both simulations commonly revealed significant dynamics of TSR3. C) The RMS fluctuations within the entire FP E244K with the trajectory aligned to the initial model illustrated by cartoon representations in which the thickness of the tube is scaled by the corresponding RMS fluctuation values per residue. D-F) Close-up of the RMS fluctuations of TSR3, TSR2 and TSR4 with the trajectories aligned to the corresponding domain, indicating that these thrombospondin repeats have limited conformational flexibility in their overall structure. Importantly, the mutation of glutamate 244 to lysine in TSR3 does not cause breakdown of the central Trp-Arg stack.

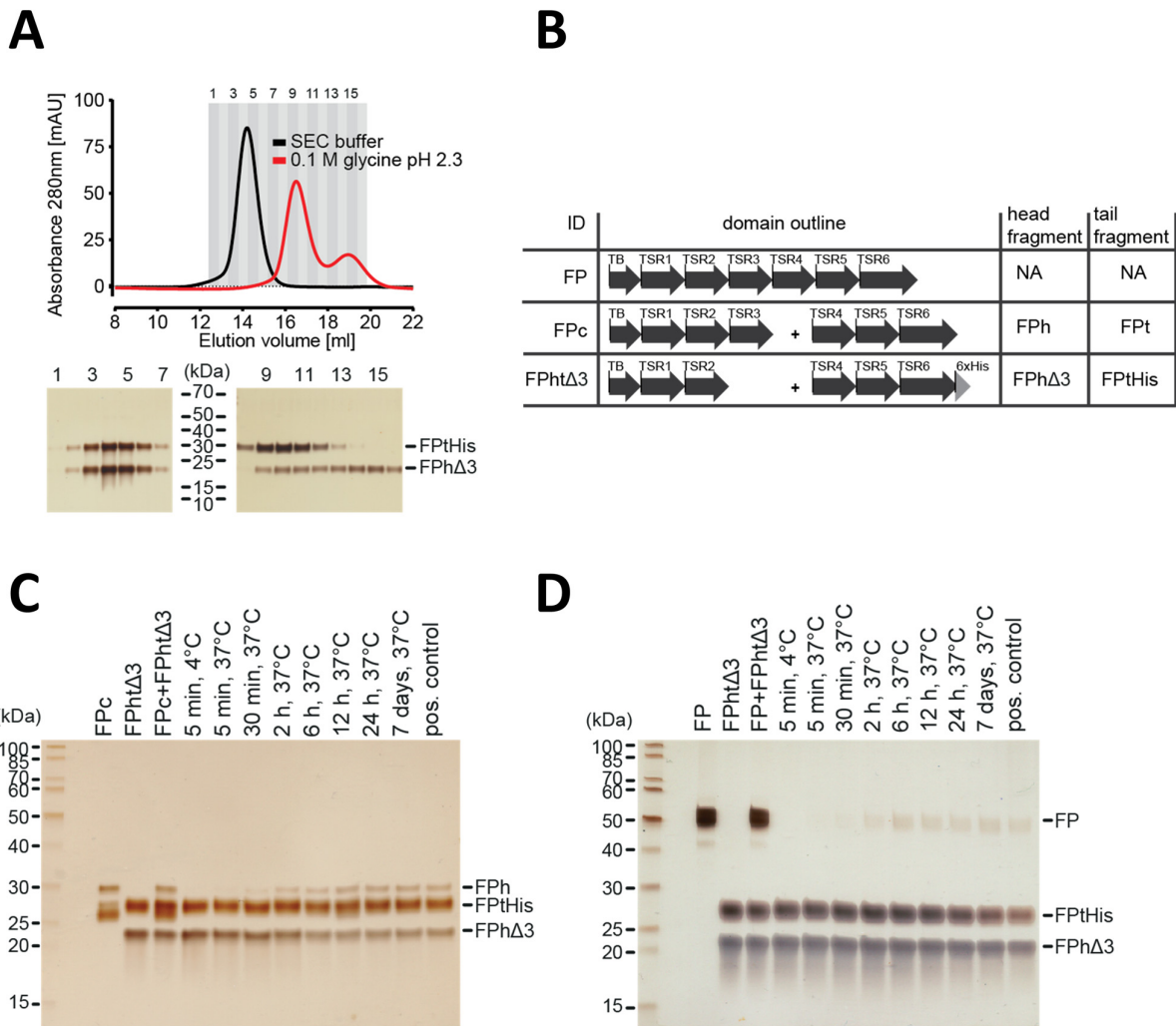


**Figure S4. FP oligomerization interfaces can open up to enable exchange monomer.** A) SEC analysis of FPhtΔ3 in 20 mM HEPES, 150 mM NaCl, pH 7.5 (black) or 100 mM glycine pH 2.3 (red), demonstrating that the two chains of FPhtΔ3 dissociate at low pH (top). Fractions from the SEC experiments were analyzed by SDS-PAGE and silver staining showing that at neutral pH the two fragments of FPhtΔ3 co-elute (bottom, left) whereas at low pH FPtHis (25 kDa) elute first and FPhΔ3 (18 kDa) elute last (bottom, right). B) Overview of FP constructs used in panels C-D. C) A silver-stained SDS-PAGE gel following the exchange of chains between FPc and FPhtΔ3. The exchange was monitored by the appearance of the FPh chain (25 kDa) from FPc and the disappearance of the FPhΔ3 chain, after pull-down on Ni-NTA beads using the His-tag on the C-terminus of FPtHis. D) A silver-stained gel from SDS-PAGE demonstrating the exchange of FP chains between FP2 and FPhtΔ3. The exchange was monitored by the appearance of the full length FP (50 kDa) after pull-down on Ni-NTA beads using the C-terminal His-tag of FPtHis from FPhtΔ3.

**Movie S1. Molecular dynamics simulation of FP E244K.** Domains and glycans are colored as in figure 1F. All frames in a 1  $\mu$ s simulation are displayed as thin lines in the background. Notice how TSR3 is able to rotate substantially around the two hinges connecting it to TSR2 and TSR4 facilitated by flexibility of the N-terminal regions in TSR3 and TSR4. The rest of the molecule exhibits only limited dynamics.

**Movie S2. Close-up on TSR3 during the MD simulation of FP E244K.** The thrombospondin repeat is shown in the orientation and coloring used in Figure S3D. Notice how the central Trp-Arg stack remains stable despite the presence of a lysine at position 244. In the structure of wild type FPc, the glutamate at position 244 engages the side chain of Arg220 in an electrostatic interaction and thereby stabilizes the arginine conformation.